This peer-reviewed article has been accepted for publication in Publications of the Astronomical Society of Australia but not yet copyedited or typeset, and so may be subject to change during the production process.

The article is considered published and may be cited using its DOI. 10.1017/pasa.2024.49

Nucleation regions in the Large-Scale Structure I. A catalogue of *cores* in nearby rich superclusters

J. M. Zúñiga,[1] C. A. Caretta,[1] and H. Andernach[1,2]

[1]Departamento de Astronomía, DCNE-CGT, Universidad de Guanajuato, Callejón de Jalisco s/n, CP 36023, Guanajuato, Gto., Mexico
[2]Currently on leave at Thüringer Landessternwarte, Sternwarte 5, D-07778 Tautenburg, Germany
Author for correspondence: J. M. Zúñiga, Email: jm.zuniga@ugto.mx.

Abstract

We applied a Density-Based Clustering algorithm on samples of galaxies and galaxy systems belonging to 53 rich superclusters from the *Main SuperCluster Catalogue* (MSCC) to identify the presence of "central regions", or *cores*, in these large-scale structures. *Cores* are defined here as large gravitationally bound galaxy structures, comprised of two or more clusters and groups, with sufficient matter density to survive cosmic expansion and virialize in the future. We identified a total of 105 galaxy structures classified as *cores*, which exhibit a high density contrast of mass and galaxies. The Density-based *Core* Catalogue (DCC), presented here, includes *cores* that were previously reported in well-known superclusters of the Local Universe, and also several newly identified ones. We found that 83% of the rich superclusters in our sample have at least one *core*. While more than three *cores* with different dynamical state are possible, the presence of a single *core* in the superclusters is more common. Our work confirms the existence of nucleation regions in the internal structure of most rich superclusters and points to the fact that these *cores* are the densest and most massive features that can be identified in the cosmic web with high probability for future virialization.

Keywords: large-scale structure of Universe, galaxies:clusters:general, catalogues, galaxies:groups:general

1. Introduction

Superclusters are the largest coherent, relatively isolated, conglomerates of galaxies that can be detected by averaging the observed –or simulated– galaxy distribution over scales of $\sim 150\ h_{70}^{-1}$ Mpc (*e.g.*, Bahcall 1996; M. Einasto et al. 2001; Liivamägi, Tempel, and Saar 2012), where h_{70} is the Hubble constant in units of 70 km s^{-1} Mpc^{-1}. These structures can be described as a hierarchical assembly of galaxies and systems (*i.e.*, groups and clusters), which are frequently connected to their neighbors by galaxy bridges (*e.g.*, J. Einasto et al. 1984), forming a complex and intricate network (the 'cosmic web', *e.g.*, Libeskind et al. 2018) of knots, filaments, walls and cosmic voids, called the Large-Scale Structure (LSS, *e.g.*, Peebles 1980; Einasto 2010) of the Universe. They can also be defined as convergent galaxy velocity fields (see, *e.g.*, Sankhyayan et al. 2023, for more details on supercluster definitions).

On the other hand, there is no theoretical or observational consensus to define the boundaries of a supercluster within the LSS, and it is even discussed whether these structures are only large transitory density enhancements in the current galaxy distribution or are really physically bound systems with established dynamics (*e.g.*, Tully et al. 2014; Böhringer, Chon, and Trümper 2021). In practice, the identification of superclusters is carried out using algorithms based mainly on techniques such as cluster analysis and percolation theory (*e.g.*, Shandarin 1983; J. Einasto et al. 1984), extended percolation (*e.g.*, J. Einasto et al. 2018), analysis of smoothed density fields or luminosity density maps (*e.g.*, Costa-Duarte, Sodré Jr., and Durret 2011; Luparello et al. 2011), and velocity field analysis (*e.g.*, Tully et al. 2014; Peñaranda-Rivera et al. 2021) among others, all combined with different empirical selection criteria (threshold density contrasts, characteristic lengths, etc).

Several catalogues of superclusters have been compiled using some of the above identification techniques: on observational samples of galaxies in large redshift surveys (*e.g.*, Einasto, Einasto, Tago, Saar, Hütsi, et al. 2007; Liivamägi, Tempel, and Saar 2012), on catalogues of systems (*e.g.*, M. Einasto et al. 2001; Chon, Böhringer, and Nowak 2013; Chow-Martínez et al. 2014), taking them as second-order galaxy agglomerations (or 'clusters of clusters', *e.g.*, Abell 1961; Bahcall and Soneira 1984), or on cosmological simulations (*e.g.*, Costa-Duarte, Sodré Jr., and Durret 2011; J. Einasto et al. 2019). In any case, superclusters appear predominantly as filamentary, planar or lumpy galaxy sets, surrounding large cosmic voids, very low-density galaxy regions of comparable size (*e.g.*, Bahcall 1996; Shandarin, Sheth, and Sahni 2004).

Some authors claim that most of the identified superclusters are not gravitationally bound structures as a whole (with internal dynamics generally dominated by the Hubble flow, *e.g.*, Pearson, Batiste, and Batuski 2014), with a rather irregular and varied morphology and rarely have well-defined "central regions" (*e.g.*, Einasto, Saar, et al. 2007; Chon, Böhringer, and Nowak 2013). Even being bound, they are assumed to be dynamically unrelaxed structures because their crossing times are of the order or higher than the age of the Universe and, thus, they still maintain the memory of their formation history (*e.g.*, Oort 1983; Chon, Böhringer, and Nowak 2013; J. Einasto

https://doi.org/10.1017/pasa.2024.49 Published online by Cambridge University Press

et al. 2019). Thus, it is still debated which of the current superclusters will survive in the future and become virialized structures (*e.g.*, Luparello et al. 2011; Chon, Böhringer, and Zaroubi 2015); it may be that only the densest and most massive clumps inside superclusters will survive the effect of the cosmic expansion and begin a process of collapse –or some may already be collapsing– as indicated by various simulations (*e.g.*, Gramann and Suhhonenko 2002; Dünner et al. 2006). Anyway, the study of the internal structure of observed superclusters can help to understand their current evolutionary states and their future within the LSS, as well as the effect of the different cosmological density environments on the evolution of their member galaxies and systems.

The filaments, long chains of galaxies and smaller galaxy systems, are the most notable features within superclusters (*e.g.*, Einasto, Saar, et al. 2007; Santiago-Bautista et al. 2020). However, in rich superclusters it is also possible to identify other prominent agglomerations of galaxies and massive systems, "central parts" (*e.g.*, M. Einasto et al. 2008; Sankhyayan et al. 2023) generally, but not necessarily, located at intersections of filaments. These regions, sometimes referred to in the literature as *cores* (*e.g.*, Bardelli et al. 1994; Small, Sargent, and Hamilton 1997; Kopylova and Kopylov 1998; M. Einasto et al. 2008; M. Einasto et al. 2015; M. Einasto et al. 2016), could be substructures in a relatively more advanced dynamical state than the rest of the supercluster and with enough mass density to gravitationally bind and collapse. The *cores* are themselves a kind of 'compact superclusters' with a higher probability of future virialization, the marginal 'island universes' (*e.g.*, Araya-Melo et al. 2009, and references therein).

Based on the hierarchical structure formation models (*e.g.*, Peebles 1980), one could expect that *cores* are structures with an intermediate dynamical state between the richest galaxy clusters and the ordinary superclusters. In other words, *cores* are for the present state of the LSS what the proto-clusters were in the past, some kind of "nucleation regions" that already have a chance to grow, collapse and virialize in our accelerated expanding Universe. In this context of continuous and unfinished structure formation, we will use indistinctly *cores* and *nucleation regions* to refer to these large, massive and relatively dense "central parts" of superclusters.

The currently massive rich clusters are found preferably at nodes of the LSS, where the network of filaments converges (e.g., M. Einasto et al. 2024). It is natural to expect that these nodes, or at least some of these, are the mere *cores*. Thus, massive systems inside superclusters could serve as markers of *cores*. The results of a preliminary study (*e.g.*, Chow-Martínez 2019) based on percolation and using the Most Massive Clusters (MMCs) of rich superclusters as "seeds" of *cores* show that about 86% of them –in an all-sky sample– may contain at least one *core*. In addition, several works have already pointed *cores* in well-studied superclusters (such as *Shapley* and *Corona-Borealis* superclusters, *e.g.*, Breen et al. 1994; Bardelli et al. 1994; Bardelli et al. 2000; Marini et al. 2004; Pearson, Batiste, and Batuski 2014, and references therein), which give us a preliminary idea of their general properties.

In this work we intend to broaden the knowledge panorama about the internal structure of superclusters in relation to the presence of *cores* and their evolutionary states. For this, we have developed a percolation-based algorithm to identify accumulations of galaxy systems within rich superclusters. The algorithm makes use of a set of search criteria (see Section 5) imposed to identify the most probable *core* candidates within each supercluster of the sample and is able to provide feedback to the user (if necessary). The study of the internal structure of superclusters provides valuable information to understand the formation and evolution of virialized structures on the largest scales. The *cores*, embedded in rich superclusters, are precisely the large-scale regions with the highest probability of future virialization, which is why they represent interesting laboratories to study the hierarchical aggregation of matter, its influence on the evolution of smaller structures within them and to test cosmological models (*e.g.*, M. Einasto et al. 2021).

This paper is organized as follows. Section 2 describes the samples of superclusters, galaxy systems and galaxies selected for our study, as well as the process for constructing the supercluster boxes to which the identification algorithms are applied. Section 3 presents the basic analysis tools used throughout this work, while the clustering algorithms (applied to galaxies and systems) for systems and structures identification, as well as for sample refinement, are discussed in Section 4. The characterization of the systems and structures is also presented in this section. Section 5 describes the method used for *core* selection from the structures identified previously. Section 6 presents the catalogue of *cores* obtained in the present study and describes some of their observational properties, comparing some of them with those reported previously in the literature. Finally, the discussion and conclusions of this work are presented in Section 7.

Through this paper a flat ΛCDM cosmology is used with the following parameters: Hubble constant $H_0 = 70\ h_{70}^{-1}$ km s^{-1} Mpc^{-1}, matter density $\Omega_m = 0.3$, curvature and radiation density $\Omega_k = \Omega_r = 0$, and dark energy density $\Omega_\Lambda = 0.7$.

2. Data

2.1 Supercluster sample

We selected a sample of 53 rich superclusters from the *Main SuperCluster Catalogue* (MSCC, Chow-Martínez et al. 2014), an all-sky catalogue containing 601 superclusters, identified by a tunable Friends-of-Friends algorithm based on a 2012 version of the spectroscopic redshift compilation of Abell/ACO-clusters (see Andernach et al. 2005, for a description), with redshifts in the interval $0.02 \leq z \leq 0.15$. The multiplicity $m_{\rm sc}$ of each MSCC-supercluster was defined as the number of its member clusters in the Abell/ACO catalogue (*e.g.*, Abell 1958; Abell, Corwin, and Olowin 1989).

https://doi.org/10.1017/pasa.2024.49 Published online by Cambridge University Press

The criteria to select the sample were: (i) choose only rich superclusters with $m_{sc} \geq 5$; (ii) select all the well-sampled superclusters inside the Sloan Digital Sky Survey (SDSS-DR13, Albareti et al. 2017), as a relatively complete subsample; and (iii) include known and well-studied superclusters of the Local Universe in the southern sky with available redshifts in the 2dF Galaxy Redshift Survey (2dFGRS, Colless et al. 2001) and the 6dF Galaxy Survey (6dFGS, Jones et al. 2009). The first criterion allows better identification of internal structures in superclusters from samples of member galaxies and systems. The second criterion provides better statistics due to the relative homogeneity of SDSS, the currently largest, densest and most complete available galaxy redshift survey, containing 116 MSCC-superclusters of all m_{sc}. Finally, the third criterion offers the possibility of having information from independent sources and including the most studied superclusters in order to be able to compare our results with those of previous studies, and to obtain validation support to our analysis.

Thus, our sample contains 45 superclusters within the SDSS region, which correspond to those selected by Santiago-Bautista et al. (2020), along with another 8 in the southern sky with a relatively good number of galaxies in the 2dFGRS or 6dFGS regions. The selected sample includes several well-known superclusters such as *Shapley*, *Pisces-Cetus*, *Ursa Major*, *Coma-Leo*, *Corona-Borealis*, *Hercules*, *Böotes*, among others. The complete sample of 53 superclusters is presented in Table 1: column 1 shows the IDs of the superclusters in the MSCC; column 2 shows their proper names when they exist; columns 3 and 4 present, respectively, the mean RA and Dec (Equinox=J2000) of the supercluster positions taken from the MSSC; column 5 shows their mean redshifts $\bar{z}$, and column 6 presents their multiplicities m_{sc}. The other columns of Table 1 will be described below.

2.2 Samples of galaxies and systems

From now on we reserve the term 'systems' to refer to first-order galaxy agglomerations such as groups and clusters, and the term 'structures' to refer to larger and second-order galaxy agglomerations (clusters of systems) such as filaments, *cores* and superclusters. Catalogues of higher density of objects make it possible to better define the systems, favoring the detection of the poorest ones and increasing the number of systems available for the detection of possible larger structures formed by them. These catalogues also improve the possibility of studying the correlations between the properties of galaxy populations and their surroundings, as well as analyzing the connectivity between member systems and substructures within superclusters. So, in order to detect *cores* in MSCC-superclusters and study their properties, it is more convenient to apply the identification algorithms on a denser and more homogeneous galaxy sample to include those systems poorer and smaller than the Abell/ACO-clusters used by Chow-Martínez et al. (2014) to compile the MSCC.

2.2.1 The SDSS galaxy sample

We use the GalCat and SysCat catalogues, compiled by Santiago-Bautista et al. (2020), to study the internal structure of superclusters within the SDSS region and the galaxy properties in these environments. The first catalogue contains all the SDSS-DR13 (*e.g.*, Albareti et al. 2017) galaxies, belonging to the SpecObj sample of extragalactic objects (*i.e.*, galaxies and low-z-quasars) with spectroscopic redshifts, inside a rectangular box that encloses each supercluster, *i.e.*, the 'supercluster box', as well as photometric (u, g, r, i, z magnitudes) and spectroscopic data from the survey. The second catalogue contains all the galaxy systems, with at least 5 members, identified by hierarchical clustering (HC, *e.g.*, Serna and Gerbal 1996; Theodoridis and Koutroumbas 2009) applied to GalCat, as well as the estimated virial properties of these systems in each supercluster box.

The SDSS-DR13 covers an area of the sky of ∼14,555 deg^2 (∼ 35% of the sky) and provides homogeneus photometric and spectroscopic data with precision of 0.1 arcsec rms and uncertainty in radial velocities of ∼30 km s^{-1} (*e.g.*, Bolton et al. 2012) of more than 2.6 million galaxies and quasars, being almost complete to the magnitude limit of the main galaxy sample (r_{pet} = 17.77) corresponding to a median redshift of $z \sim 0.1$. Thus, the SDSS-DR13 is a suitable database for the identification of galaxy systems and structures in the LSS and the study of galaxy properties in different cosmological environments. The GalCat and SysCat catalogues were used successfully by Santiago-Bautista et al. (2020) to identify filaments in MSCC-superclusters.

2.2.2 Southern galaxy sample

For superclusters located outside the SDSS region we compiled catalogues analogous to GalCat and SysCat (see the procedure below), but taking galaxies from the 2dFGRS or 6dFGS surveys (or just 2dF and 6dF for short), depending on where each of these superclusters had higher number density and greater coverage and homogeneity of galaxies. Both redshift surveys have also been quite useful and historically important for the study of the distribution of galaxies in the LSS.

The 2dF survey provides reliable redshifts for 221,414 galaxies brighter than an extinction-corrected nominal magnitude limit of b_J = 19.45 ($r_F \sim 18.3$ for early-type or $r_F \sim 18.6$ for late-type galaxies, *e.g.*, Cole et al. 2005), covering an area of ∼1,500 deg^2 (only ∼ 4% of the sky) in regions of high Galactic latitude in both the northern and southern Galactic hemispheres and with median redshift of z = 0.11. The four superclusters of our sample inside this database are all in the southern hemisphere.

The 6dF survey offers a catalogue of 125,071 galaxies, making near-complete samples with magnitude limits $K \leq 12.65$, $H \leq 12.95$, $J \leq 13.75$, $r_F \leq 15.60$, and $b_J \leq 16.75$ (e.g., Jones et al. 2009), for almost half of the sky (∼17,000 deg^2 on the southern sky, $|b| > 10$ deg), with a median redshift of z = 0.053.

https://doi.org/10.1017/pasa.2024.49 Published online by Cambridge University Press

Table 1. Sample of MSCC-superclusters

ID MSCC	Name[1]	RA [deg]	Dec [deg]	$\bar{z}$	m_{sc}	$N_{\mathcal{G}box}$	N_{sys}	Survey	ε_{sc} [h_{70}^{-1} Mpc]	$N_{\mathcal{G}sc}$
(1)	(2)	(3)	(4)	(5)	(6)	(7)	(8)	(9)	(10)	(11)
1	Pisces-Cetus (Southern)	0.77	-26.72	0.064	9	6567	114	2dF	13.7	5891
27	Pisces-Cetus (Central)	11.32	-22.87	0.061	9	2602	34	2dF	13.7	2306
33	Sculptor	13.02	-26.68	0.112	24	8893	137	2dF	12.5	6346
39	Pisces-Cetus (Northern)	14.65	-11.34	0.054	11	1241	15	6dF	18.2	736
55		17.73	15.43	0.061	5	812	16	SDSS	13.9	519
72		25.19	0.63	0.080	5	1941	50	SDSS	16.9	1670
75		28.09	-5.15	0.094	7	1607	16	SDSS	26.0	1182
76		28.36	-2.61	0.130	16	2617	25	SDSS	28.5	1982
117	Horologium-Reticulum	49.89	-48.46	0.066	26	2848	25	6dF	18.7	1448
175		125.30	17.07	0.094	6	2504	33	SDSS	17.1	1884
184		130.10	30.23	0.106	6	2101	19	SDSS	23.0	1457
211		147.87	64.87	0.119	8	1484	5	SDSS	20.9	619
219		153.99	19.13	0.116	5	1913	21	SDSS	22.7	1635
222		155.15	49.20	0.138	10	1865	16	SDSS	19.5	1127
223		155.24	62.94	0.140	5	776	4	SDSS	19.3	222
229		156.15	33.03	0.142	7	1855	8	SDSS	36.3	1291
236		156.77	10.37	0.033	6	8636	162	SDSS	9.9	7299
238		156.98	39.54	0.107	21	8328	106	SDSS	25.9	6815
248		159.49	44.26	0.125	5	1263	7	SDSS	27.0	823
264		165.30	12.20	0.116	8	1704	23	SDSS	24.8	1322
266		165.91	11.84	0.127	8	958	9	SDSS	17.3	502
272		167.85	41.33	0.076	6	1379	15	SDSS	16.6	1126
277		169.40	49.66	0.110	7	2748	24	SDSS	18.4	1756
278	Leo	169.40	28.46	0.033	6	7920	113	SDSS	14.9	7387
283		170.79	20.33	0.138	12	2320	24	SDSS	24.8	1490
295	Coma-Leo	173.60	23.12	0.022	5	14308	153	SDSS	10.0	12182
310	Ursa Major	175.88	55.24	0.064	21	12286	244	SDSS	12.4	10228
311	Virgo-Coma A	176.15	9.90	0.083	8	5270	81	SDSS	19.1	4551
314		177.14	-2.00	0.079	6	558	13	SDSS	8.9	405
317		177.47	-1.58	0.128	13	840	14	SDSS	18.6	658
323		179.67	27.25	0.140	12	3330	35	SDSS	17.7	1722
333		181.43	29.32	0.081	9	1968	40	SDSS	8.1	1066
335		182.41	29.48	0.073	6	3099	65	SDSS	12.1	2138
343	Virgo-Coma B	183.89	14.30	0.081	5	2679	44	SDSS	9.1	1706
360	Draco	190.93	64.40	0.106	11	2199	28	SDSS	22.4	1944
386		199.53	38.31	0.072	5	3256	68	SDSS	16.2	2671
389	Shapley	201.05	-32.89	0.049	24	4649	79	6dF	16.9	3790
407		208.56	26.70	0.136	6	1126	10	SDSS	23.3	635
414	Boötes	211.30	27.33	0.071	24	10902	293	SDSS	10.4	9012
419		212.34	7.17	0.112	5	1723	44	SDSS	15.4	1340
422		213.21	28.95	0.143	9	1065	8	SDSS	35.2	821
430		216.72	25.64	0.098	6	1603	27	SDSS	16.5	1303
440	Boötes A	223.17	22.27	0.117	9	3442	38	SDSS	20.7	2617
441		223.22	28.39	0.125	5	1058	5	SDSS	28.5	646
454		228.26	7.18	0.046	6	5704	185	SDSS	15.2	5590
457		228.61	6.97	0.079	6	4072	97	SDSS	18.6	3819
460		229.69	31.16	0.114	9	3499	50	SDSS	15.6	2598
463	Corona Borealis	232.20	30.42	0.074	14	8466	223	SDSS	10.8	7126
474	Hercules	241.50	16.22	0.036	5	7424	92	SDSS	9.9	6623
484		245.58	42.39	0.136	7	1319	9	SDSS	9.1	242
509	Pavo-Indus	311.70	-39.98	0.023	6	3008	51	6dF	17.3	2584
574	Aquarius B	348.10	-21.69	0.122	42	5982	65	2dF	19.3	4020
579		351.75	14.79	0.043	5	1477	40	SDSS	15.5	1190

Table note

1 Taken from M. Einasto et al. (2001), Chow-Martínez et al. (2014), Santiago-Bautista et al. (2020), and references therein.

https://doi.org/10.1017/pasa.2024.49 Published online by Cambridge University Press

Although 6dF covers a larger area of the sky ($\sim$ 41%), it is shallower than 2dF and SDSS, allowing to cover only four MSCC-superclusters with $z \leq 0.08$ in our sample.

To build the supercluster boxes we first transform the redshift-angular coordinates of 2dF/6dF galaxies and Abell/ACO-clusters to rectangular coordinates. Thus, if (α, δ) are the equatorial coordinates (RA and Dec) of a galaxy or system, its rectangular coordinates can be estimated in the form

$$\begin{aligned} X &= D_c \cos\delta \cos\alpha, \\ Y &= D_c \cos\delta \sin\alpha, \\ Z &= D_c \sin\delta, \end{aligned} \tag{1}$$

where,

$$D_c(z) = \frac{c}{H_0} \int_0^z \frac{dz'}{E(z')}, \tag{2}$$

is the line-of-sight comoving distance (*e.g.*, Hogg 2000) of the object defined by its redshift z, c is the speed of light, and

$$E(z) \equiv \sqrt{\Omega_r(1+z)^4 + \Omega_m(1+z)^3 + \Omega_k(1+z)^2 + \Omega_\Lambda}. \tag{3}$$

Then, in a similar way as in Santiago-Bautista et al. (2020), we take all the 2dF/6dF galaxies located within the corresponding rectangular volume box that encloses the member Abell/ACO-clusters of each supercluster, including those found up to a distance of 20 h_{70}^{-1} Mpc beyond the center of the farthest member cluster in each direction. For each supercluster box, we compile the southern GalCat catalogue containing the equatorial coordinates (FK5, Equinox=J2000.0), the redshift and the magnitudes of each galaxy. For 2dF galaxies we select the final b_J magnitude corrected from extinction and the SuperCosmos R magnitude (*e.g.*, Hambly et al. 2001), while for 6dF galaxies we select the recalibrated b_J and r_F magnitudes (*e.g.*, Cole et al. 2005). Photometric and spectroscopic data were taken directly from the 2dF and 6dF catalogues, both available in VizieR[a]. In each supercluster box, a system detection algorithm was applied to build the corresponding southern SysCat. The details of this algorithm are described in Section 4. The left panel of Figure 4 below shows, for example, the raw supercluster box for the *Shapley Supercluster* (MSCC 389 and MSCC 401) extracted from 6dF.

Columns 7 and 8 of Table 1 show, respectively, the number $N_{g_{\rm box}}$ of galaxies (GalCat) and the number $N_{\rm sys}$ of detected galaxy systems (SysCat) within each supercluster box either from Santiago-Bautista et al. (2020) or the ones we detected from 2dF or 6dF; column 9 shows the survey from which the galaxy sample for each supercluster was drawn. In most cases, the number of systems identified within each supercluster box (in any of the SDSS, 2dF or 6dF regions) significantly exceeds the number of its member Abell/ACO-clusters (compare columns 6 and 8 of Table 1).

a. see https://cdsarc.cds.unistra.fr/viz-bin/cat/VII/250 and https://cdsarc.cds.unistra.fr/viz-bin/cat/J/MNRAS/399/683.

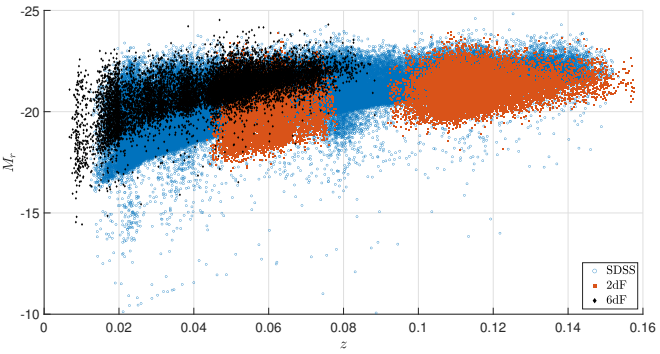

Figure 1. Distribution of M_r galaxy absolute magnitudes as a function of redshift. Included here are the three galaxy samples taken from the SDSS (blue circles), 2dF (red boxes) and 6dF (black diamonds) Surveys.

2.2.3 *Luminosity limits of the sub-samples*

Although the three sub-samples are not homogeneous in depth, they were selected to identify galaxy systems with enough membership completeness for estimating their dynamical parameters necessary for our study. Figure 1 shows the absolute magnitudes M_r of our total sample (SDSS + 2dF + 6dF sub-samples) of galaxies as a function of redshift.

For SDSS, the faint limit for M_r is mainly due to $r_{\rm pet}$ = 17.77, which corresponds to SDSS DR7 data, while we used SDSS DR13 which contains spectra for some fainter objects below this limit. This apparent magnitude limit corresponds to $M_r - 5log(h) = -20.7$, or $M_r = -21.5$ for our assumed cosmology, at the redshift limit of our sample. This corresponds to about M_r^* for early-type galaxies (*e.g.,* Nakamura et al. 2003). For 2dF, the limit in apparent magnitudes is fainter and less sharp ($r_F \sim 18.3$, corresponding to $M_r = -21.0$, taking color correction from r_F to r to be very small), a limit slightly fainter than the one for SDSS as be seen for the two red patches along the z axis ($0.045 \leq z \leq 0.075$ and $0.095 \leq z \leq 0.150$) that cover our used data. The case of 6dF (black points) is particular: since this survey is much shallower than the others, having a limiting apparent magnitude of only $r_F \sim 15.6$, we used these data only to study nearby superclusters ($z \leq 0.08$, which correspond to a luminosity limit of $M_r = -22.2$). Thus, in the worst case of the redshift limits of our sample we have at least galaxies brighter than M_r^* as potential members of the galaxy systems we detect. This is important to guarantee that the calculated dynamical parameters are reliable for our analysis. We will come back to the discussion of uncertainties in dynamical parameters below.

3. Analysis tools

The methodology used in the present work was divided in 3 sections: the basic analysis tools, the clustering algorithms and characterization of systems and structures, and the strategy to identify the *cores*. Here, we start with the basic tools.

https://doi.org/10.1017/pasa.2024.49 Published online by Cambridge University Press

3.1 Distances and projection angle

For two galaxy systems observed with angular separation θ_{jk} (in radians) and redshifts z_j and z_k, the physical distance r_{jk} between them and their projected separation R_{jk} in the sky-plane (both defined in units of h_{70}^{-1} Mpc) are given, respectively, by

$$r_{jk} = \sqrt{D_c^2(z_j) + D_c^2(z_k) - 2D_c(z_j)D_c(z_k)\cos\theta_{jk}}, \quad (4)$$

and,

$$R_{jk} \simeq \theta_{jk} D_A(\bar{z}) = \theta_{jk} \frac{D_c(\bar{z})}{1+\bar{z}}, \quad (5)$$

where $D_A(z)$ is the angular diameter distance (*e.g.*, Hogg 2000), and $\bar{z}$ the average redshift of the systems.

Furthermore, if $z_j \leq z_k$, the tangent of the projection angle χ between the separation vector along r_{jk} and the sky-plane, at the midpoint between the pair of systems, is

$$\tan\chi = \frac{z_k - z_j}{2z_j \tan(\theta_{jk}/2)}, \quad (6)$$

with $0 \leq \chi \leq \pi/2$ (*e.g.*, Sargent and Turner 1977). As can be seen below, this angle can be used to test the dynamical state of the pair of systems.

3.2 Binding Tests

3.2.1 Pairwise gravitational binding

Consider two galaxy systems of masses m_j and m_k, with redshifts $z_j \leq z_k$ and separated by a distance r_{jk}. Assuming linear orbits for the systems, *i.e.*, with no rotations or discontinuities around the center of mass, one can use the Newtonian energy criterion, $v_{jk}^2 \leq 2G\mathcal{M}/r_{jk}$, where v_{jk} is the relative velocity between systems, G the universal gravitational constant and $\mathcal{M} = m_j + m_k$ the pair total mass, to check the state of gravitational binding of the pair (*e.g.*, Beers, Geller, and Huchra 1982). Thus, since $R_{jk} = r_{jk}\cos\chi$ is the projected separation (in the sky-plane) between systems, and $v_{r_{jk}} = v_{jk}\cos\chi \approx H_0\ r_{jk}$ their relative radial velocity, then the pair binding criterion can be evaluated observationally in the form:

$$v_{r_{jk}}^2 R_{jk} \leq 2G\mathcal{M}\sin^2\chi\cos\chi. \quad (7)$$

3.2.2 Gravitationally bound structures

An alternative method can be tested to check the gravitational binding state of a 'cluster of systems' as a whole, if the individual masses the member systems are known. A structure composed of N objects of masses m_j, peculiar velocities v_j with respect to its center of mass, and relative separations r_{jk} between them, will be gravitationally bound if $K \leq |W|$, where K and W are the internal kinetic and potential energies, respectively, so that

$$\frac{1}{2}\sum_{j=1}^{N} v_j^2 m_j \leq \frac{1}{2}\sum_{j\neq k}^{N} \frac{Gm_j m_k}{r_{jk}}. \quad (8)$$

The above inequality can be expressed in the observationally more practical form (*e.g.*, Schneider 2015):

$$\frac{1}{2}\sigma_{\rm sys}^2 \leq \frac{G\mathcal{M}}{r_G}, \quad (9)$$

where $\sigma_{\rm sys}^2 := \langle v_i^2 \rangle$ is the squared velocity dispersion of systems inside the structure, $\mathcal{M} := \sum m_k$, and

$$r_G := 2\mathcal{M}^2 \left(\sum_{i\neq j} \frac{m_j m_k}{r_{jk}} \right)^{-1}, \quad (10)$$

is the gravitational radius of the structure.

Since only the line-of-sight (radial) component of the velocity, v_{r_j}, can be estimated for each galaxy system, one can, to a first approximation, assume that $\sigma_{\rm sys}^2 = \beta \left\langle v_{r_j}^2 \right\rangle$, with $\beta \approx 3$ assuming a quasi-Maxwellian distribution of peculiar velocities of the systems inside the structures (see Bahcall 1996) or $\beta \approx 2.5$ asuming a weak anisotropy in the system velocity distributions (similar to that used for galaxy velocity distributions, *e.g.*, Tully 2015). Thus, the binding condition (9) can be evaluated in the form

$$\beta\sigma_{v_{\rm sys}}^2 r_G \leq 2G\mathcal{M}, \quad (11)$$

where, $\sigma_{v_{\rm sys}}^2 = \left\langle v_{r_j}^2 \right\rangle$ is the line-of-sight squared velocity dispersion of galaxy systems inside the structure.

3.3 Future virialized structures

Following the strategy adopted by Dünner et al. (2006), Chon, Böhringer, and Zaroubi (2015) and references therein, and thinking of each galaxy structure as an overdense region of mean mass density $\rho_{\rm ov}$, one can define the ratio

$$\mathcal{R} \equiv \frac{\rho_{\rm ov}}{\rho_{\rm b}}, \quad (12)$$

between the overdensity and the local background[b] mean mass density $\rho_{\rm b}$, as well as the the density contrast

$$\Delta_{\rm cr} \equiv \frac{\rho_{\rm ov}}{\rho_{\rm cr}} - 1, \quad (13)$$

of the overdensity with respect to the critical density of the Universe, $\rho_{\rm cr} = 3H^2(z)/8\pi G$, where $H(z) = H_0 E(z)$ is the Hubble parameter, *i.e.*, the Hubble constant at redshift z.

It is possible to use physically motivated density criteria to decide which structures –on scales of superclusters or *cores*– will be able to survive the cosmic expansion and become virialized systems in the future. Assuming spherically symmetric overdense regions, the density criteria are based on theoretical estimates of the mean density that must be enclosed by its last

b. see Section 5.3 for more details on the estimation of $\rho_{\rm b}$ here.

https://doi.org/10.1017/pasa.2024.49 Published online by Cambridge University Press

–or 'critical'– shell, at a given cosmological epoch, so that it remains gravitationally bound to the overdensity in a future dominated by dark energy (*e.g.*, Chiueh and He 2002; Łokas and Hoffman 2002; Dünner et al. 2006). Using the spherical collapse model in an ΛCDM scenario, Chon, Böhringer, and Zaroubi (2015) estimated, for various cosmologies, threshold values for $\mathcal{R}$ and $\Delta_{\rm cr}$ that characterize structures that are currently at turn-around (*i.e.*, structures that have already decoupled from the Hubble flow and are at rest in the Eulerian frame of reference, so they are now beginning to collapse, Chon, Böhringer, and Zaroubi 2015) compared to those that will collapse marginally. Likewise, Dünner et al. (2006) estimated very consistent values at the current time for $\mathcal{R}$ and $\Delta_{\rm cr}$ within the last layer that will eventually stop its expansion. The threshold values of these two parameters are shown in Table 2.

Although the threshold values for $\mathcal{R}$ and $\Delta_{\rm cr}$ parameters are valid only for spherical overdensities, they are approximately reasonable for other realistic structures: these density criteria have been successfully used to define *bound structures* in future extended N-body cosmological simulations (Dünner et al. 2006); to build catalogues of zones —from the SDSS-DR7 region— that will become *future virialized structures* (FVSs, Luparello et al. 2011); to study whether currently known superclusters will survive cosmic expansion (the *superstes-clusters*, Chon, Böhringer, and Zaroubi 2015); and to identify and study the properties of *quasi-spherical superclusters* also in SDSS-DR7 region (*e.g,* Heinämäki et al. 2022). As stated in Sankhyayan et al. (2023), a definition of "superclusters" based on large gravitationally bound structures most often leads to the identification of the central regions of the superclusters identified by other criteria like overdensities in galaxy or light distribution and converging peculiar velocity fields regions. Thus, the *cores* we define here may not be confused with ordinary superclusters, but are a generalization of the bound or future virialized structures described above.

Table 2. Current-epoch threshold values for density ratio ($\mathcal{R}$) and density contrast ($\Delta_{\rm cr}$) characterizing structures at turn-around and those that are marginally collapsing, assuming a flat cosmology with $\Omega_{m,0} + \Omega_{\Lambda,0} = 1$, where $\Omega_{m,0} = 0.3$, $\Omega_{\Lambda,0} = 0.7$ and $h_{70}^{-1} = 0.7$.

Reference	at turn-around		future collapse	
	$\mathcal{R}$	$\Delta_{\rm cr}$	$\mathcal{R}$	$\Delta_{\rm cr}$
Dünner et al. 2006	-	-	7.88	1.36
Chon et al. 2015	12.15	2.65	7.86	1.36

3.4 Percolation and FoF algorithm

The galaxy clustering, present in a hierarchical way at different scales, can be studied by percolation theory (*e.g.*, Stauffer 1979; Shandarin 1983), introduced in cosmological studies by Zeldovich, Einasto, and Shandarin (1982), Melott et al. (1983) and J. Einasto et al. (1984). In this context, the set of coordinates of galaxies and/or systems constitutes the point distribution space where the clustering will be analyzed.

The well-known Friends-of-Friends (FoF) algorithm is a percolation technique that uses a single input parameter, the *linking length* ε, as a distance criterion to link points and detect agglomerates in a data space: two points p and q are linked to each other ('friends') if the distance between them is $d_{pq} \leq \varepsilon$; also a third point s, such that $d_{ps} > \varepsilon$, is linked to both p and q if $d_{qs} \leq \varepsilon$ ('friend of friend'). The set of all points that are mutually friend constitute a 'cluster'. We will use the term 'cluster', in quotes, to refer to any agglomeration of points in a generic data space and avoid confusion with conventional clusters of galaxies. If ε is very small, the number of 'clusters' will be reduced to those with the highest density of points. As ε gets large, the dense 'clusters' will begin to link to each other through their boundary points and sparse points in the data volume, so the number of detected 'clusters' will begin to decrease until, on some large scale, the entire sample percolates (*e.g.*, J. Einasto et al. 1984). The value $\varepsilon = \varepsilon_c$ for which the number of detected 'clusters' in the percolation process is maximized is called critical linking length (or critical percolation radius, *e.g.*, Shandarin 1983; Chow-Martínez et al. 2014).

The FoF technique is attractive, among other things, because it produces a single 'cluster' catalogue for each linking volume and does not assume any particular shape or geometry for the 'clusters' (*e.g.*, Berlind et al. 2006). In astronomy, the FoF algorithm has often been used to detect galaxy clusters in redshift surveys (*e.g.*, Huchra and Geller 1982; Berlind et al. 2006), superclusters or filamentary structures in samples of galaxies and clusters (*e.g.*, J. Einasto et al. 1984; M. Einasto et al. 2001; Caretta et al. 2002; Chow-Martínez et al. 2014), and identify dark matter halos in N-body simulations (*e.g.*, Davis et al. 1985).

3.5 The DBSCAN algorithm

Density-Based Clustering is a family of unsupervised learning methods capable of identifying distinctive 'clusters' in a data space. The method is based on the idea that a 'cluster' is a region of high density of points, separated from other 'clusters' by neighboring regions of low density of points, typically considered noise/outliers (*e.g.*, Sander 2011; Kriegel et al. 2011). In this work we use the Density-Based Spatial Clustering of Applications with Noise (DBSCAN, Ester et al. 1996), one of the most popular and cited clustering algorithms in the scientific literature. This algorithm is advantageous because it does not require knowing, as an input parameter, the number k of 'clusters' to be detected (unlike *k-means* or *k-medoid* algorithms). Rather, it determines this parameter automatically from the data set ($\mathcal{D}$), the radius of the neighborhood around each point (ε), and the minimum number of points in each 'cluster' ($N_{\rm min}$). Once the input parameters ($\mathcal{D}, \varepsilon, N_{\rm min}$) are established, DBSCAN searches for 'clusters' according to the following definitions:

Definition 1: (ε-neighborhood) The *ε-neighborhood* of a point p, denoted by $N_\varepsilon(p)$, is defined by $N_\varepsilon(p) = \{q \in \mathcal{D} | d_{pq} \leq \varepsilon\}$,

https://doi.org/10.1017/pasa.2024.49 Published online by Cambridge University Press

where d_{pq} is the distance between p and q.

Definition 2: (directly density-reachable) A point p is *directly density-reachable* from a point q with respect to ε and $N_{\min}$ if: (i) $p \in N_\varepsilon(q)$ and, (ii) $|N_\varepsilon(q)| \geq N_{\min}$.

Definition 3: (density-reachable) A point p is *density-reachable* from a point q with respect to ε and $N_{\min}$ if there is a chain of points $p_1, ..., p_n$, $p_1 = q$, $p_n = p$ such that p_{i+1} is directly density-reachable from p_i.

Definition 4: (density-connected) A point p is *density-connected* to a point q with respect to ε and $N_{\min}$ if there is a point s such that both, p and q are density-reachable from s with respect to ε and $N_{\min}$.

Definition 5: ('cluster') Let $\mathcal{D}$ be a database of points. A *'cluster' C* with respect to ε and $N_{\min}$ is a non-empty subset of $\mathcal{D}$ satisfying the following conditions: (i) $\forall p, q$: if $p \in C$ and q is density-reachable from p wrt. ε and $N_{\min}$, then $q \in C$; (ii) $\forall p, q \in C$: p is density-connected to q with respect to ε and $N_{\min}$.

Definition 6: (noise) Let $C_1, ..., C_k$ be the 'clusters' of the database $\mathcal{D}$ with respect to parameters ε_i and $N_{\min_i}$, $i = 1, ..., k$. Then the *noise* is defined as the set of points in the database $\mathcal{D}$ not belonging to any cluster C_i, *i.e.* noise = $\{p \in \mathcal{D} | \forall i : p \notin C_i\}$.

As a result, DBSCAN allows to discover 'clusters' with arbitrary shapes (spherical, linear, elongated, etc., depending on the chosen d_{pq} metric function), using few input parameters and with good efficiency in large databases (see Ester et al. 1996), so that it can be successfully used for astronomical analysis. The DBSCAN technique is basically a percolation-based algorithm for linking points, supplemented with sufficient density criteria to define agglomerates and noise. A similar extended percolation method using the density field instead of points was used by J. Einasto et al. (2018) to study the connectivity of over- and under-dense regions in the cosmic web.

4. Clustering analysis

4.1 Detection of galaxy systems in the southern sample

The detection of systems in superclusters (from the 2dF or 6dF regions) to compile the southern SysCat catalogue was performed by an automated algorithm based on those presented by Biviano et al. (2006) and Santiago-Bautista et al. (2020), executing the following steps in each box:

(1) The galaxies in the supercluster box were represented by the set of points with coordinates $\mathcal{D} = \{(\alpha_k, \delta_k, 1000 z_k),\ k = 1, ..., N_{g_{\rm box}}\}$, compiled in its southern GalCat catalogue. The factor of 1000 was applied to redshift z values to be comparable to the sky coordinate values α and δ. The set of points in this form represents a pseudo-three-dimensional space where the –dimensionless- distances can be estimated with the metric

$$d_{jk} = \sqrt{(\Delta\alpha_{jk} \cos\bar{\delta})^2 + (\Delta\delta_{jk})^2 + (1000\Delta z_{jk})^2} \qquad (14)$$

where $\Delta\alpha_{jk} = \alpha_j - \alpha_k$, $\Delta\delta_{jk} = \delta_j - \delta_k$, $\Delta z_{jk} = z_j - z_k$ and $\bar{\delta}$ is the mean declination between galaxies j and k.

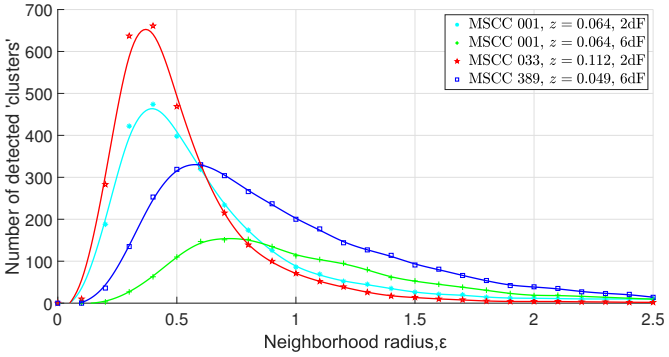

Figure 2. Percolation curves (PCs) obtained for three superclusters sampled in the 2dF or 6dF region, using galaxies as input data. The PCs show the variation in the number of first-order galaxy 'clusters', with $N_{\min} = 3$ galaxies, detected by the DBSCAN algorithm as the neighborhood radius varies. The lines represent the smoothing-spline of data and their maxima are located at the critical neighborhood radius, ε_c.

(2) A DBSCAN-based algorithm, with input parameters $(\mathcal{D}, \varepsilon, 3)$, was applied iteratively for a wide range of neighborhood radii, $0 \leq \varepsilon \leq 2.5$, to analyze the percolation properties of galaxies and determine the –dimensionless– critical neighborhood radius ε_c.

Figure 2 shows an example of four percolation curves (PCs, *i.e.*, number of detected 'clusters' *vs.* neighborhood radius) obtained for three superclusters. The PCs were obtained with the data from the best box (in 2dF or 6dF) for each supercluster, except for one of them where the PCs were obtained with the data from both boxes (in 2dF and 6dF) for comparison. It can be seen that, in addition to its dependence on redshift, the radius ε_c depends on factors such as the density and homogeneity of the survey in the region of a given supercluster. The critical neighborhood radii obtained for the 8 superclusters in the 2dF and 6dF regions have mean and median values of 0.6 and 0.5, respectively, similar to the dimensionless neighborhood radius value obtained by J. Einasto et al. (1984) to detect galaxy clusters (and groups) by FoF.

(3) The radius ε_c was established as the most appropriate to find 'clusters' with $N_{\min} = 3$ in the box. The projected centroid, $c_i = (\alpha_i, \delta_i)$, and line-of-sight (radial) velocitiy, v_{r_i}, of each detected i-'cluster' was initially estimated as median values of its member galaxies. Not all the 'clusters' identified in this step are necessarily physical galaxy systems, but around their positions it is more likely to find them.

https://doi.org/10.1017/pasa.2024.49 Published online by Cambridge University Press

(4) All galaxies contained within an initial projected aperture $R_{a_i} = 1\ h_{70}^{-1}$ Mpc from each centroid c_i and whose radial velocities were in the interval $\upsilon_{r_i} \pm 3S_a$, with $S_{a_i} = 1000$ km s^{-1}, were taken. That is, galaxy cylinders oriented along the line-of-sight in redshift space with radius R_{a_i} and depth $6S_{a_i}$ were taken centered on (c_i, υ_{r_i}).

(5) The cylinders with 5 or more galaxies were accepted as candidates for galaxy systems, while the others were rejected. For these candidates, line-of-sight velocities V_{LOS_i} and velocity dispersions σ_{υ_i} were estimated using Tukey's biweight method (see Beers, Flynn, and Gebhardt 1990), and centroids were recalculated.

(6) The virial mass of each candidate within the cylinder was determined as (*e.g.*, Biviano et al. 2006; Tully 2015):

$$\mathcal{M}_{\mathrm{vir}_i} = \frac{\beta\pi}{2G}\sigma^2_{\upsilon_i} R_{\mathrm{vp}_i}, \tag{15}$$

with β being, as above, an anisotropy parameter for the galaxy velocity distributions, and R_{vp_i}, the projected mean radius, calculated in the form

$$R_{\mathrm{vp}_i} = \frac{N_i(N_i-1)}{\sum_{j<k} 1/R^{(i)}_{jk}}, \tag{16}$$

where $R^{(i)}_{jk}$ is the projected distance (in the sky-plane) between pairs of galaxies and N_i the number of them within the i-th cylinder. Furthermore, assuming a spherical model for nonlinear collapse with virialization density $\rho_{\mathrm{vir}} = 18\pi^2[3H^2(z)/8\pi G]$ (*e.g.*, Bryan and Norman 1998), the virial radius is then

$$r^3_{\mathrm{vir}_i} = \frac{3\mathcal{M}_{\mathrm{vir}_i}}{4\pi\rho_{\mathrm{vir}_i}} = \frac{\beta\sigma^2_{\upsilon_i} R_{\mathrm{vp}_i}}{18\pi H^2(z_i)}. \tag{17}$$

(7) For each candidate, the aperture R_{a_i} was updated to the corresponding calculated r_{vir_i} value, the median radial velocity v_{r_i} to V_{LOS_i}, and S_a to σ_{υ_i}, defining a new cylinder (including or excluding galaxies as the case may be). The process, from step (4) to (7), was repeated iteratively unti finding the $r_{\mathrm{vir}_i} \sim R_{a_i}$ convergence.

Here, we assume an $r_{\mathrm{vir}_i} \sim R_{a_i}$ convergence when

$$\frac{|r_{\mathrm{vir}_i} - R_{a_i}|}{R_{a_i}} \leq 0.05, \tag{18}$$

that is, if the relative difference between r_{vir_i} and R_{a_i} was less than or equal to 5%.

(8) The candidates for which r_{vir_i} converged before 20 iterations were accepted as real galaxy systems and their dynamical properties correspond to those estimated at the end of the last iteration, while those that did not converge were rejected. All the systems for which convergence $r_{\mathrm{vir}_i} \sim R_{a_i}$ occurred achieved it well before 20 iterations.

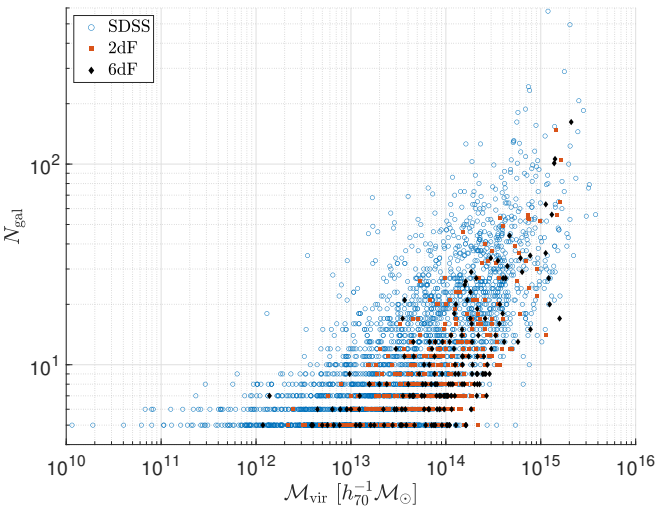

Figure 3. Richness as a function of mass for the complete sample of 3,337 SysCat systems identified in the SDSS, 2dF, and 6dF regions.

Accepted systems become part of the corresponding southern SysCat catalogue of the respective supercluster, indicating for each member system its centroid (RA, Dec, $\bar{z}$), position of its Brightest Cluster Galaxy (BCG), the number of member galaxies (N_g), its line-of-sight velocity (V_{LOS}), its radial galaxy velocity dispersion (σ_υ), its virial mass ($\mathcal{M}_{\mathrm{vir}}$) and its projected ($R_{\mathrm{vp}}$) and virial ($r_{\mathrm{vir}}$) radii.

Figure 3 shows the distribution of richness versus mass for our total sample of 3,337 SysCat systems (*i.e.*, combining those identified in the SDSS, 2dF and 6dF regions). This distribution is very similar to the one obtained by Tempel et al. (2014) for systems with $N_{\mathrm{gal}} \geq 5$.

4.1.1 *FoG-effect correction*

For each accepted system, a simple correction for the Finger-of-God effect (FoG, *e.g.*, Coil 2012) was performed by adjusting the position of its member galaxies in the final cylinder, so that their comoving distances were rescaled to stay within the calculated virial radius. Thus, if $D_{\mathrm{c}_k} = D_{\mathrm{c}}(z_k)$ is the initial comoving distance of the k-th member galaxy, at redshift z_k, in the i-th system, its rescaled comoving distance is

$$D'_{\mathrm{c}_k} = \frac{2r_{\mathrm{vir}_i}}{\epsilon}\left(D_{\mathrm{c}_k} - D^{(i)}_{\mathrm{c}}\right) + D^{(i)}_{\mathrm{c}}, \tag{19}$$

where $D^{(i)}_{\mathrm{c}} = D_{\mathrm{c}}(V_{\mathrm{LOS}_i}/c)$ is the comoving distance to the centroid of the system, and $\epsilon = \max_k\{D_{\mathrm{c}_k}\} - \min_k\{D_{\mathrm{c}_k}\}$, with $k = 1, ..., N_i$, is the distance (in the line of sight) between the nearest and the most distant galaxy in the system. The surface pressure term correction based on the concentration parameter was not applied here, however a virial approximation is sufficient for the objective of this work (*e.g.*, Santiago-Bautista et al. 2020).

The FoG-effect can be seen in the three-dimensional distribution of galaxies obtained by transforming their coordinates

https://doi.org/10.1017/pasa.2024.49 Published online by Cambridge University Press

from raw redshift-angular (provided by the source survey) to rectangular directly through eq. (1), as shown in the left panel of Figure 4 for the *Shapley Supercluster*. The regions of red points are galaxy systems which appear elongated in the line-of-sight due to the effect of the peculiar velocities of member galaxies (*e.g.*, Coil 2012). After the FoG-correction, re-estimating the rectangular coordinates only for member galaxies of systems using the rescaled comoving distances from eq. (19) in eq. (1), the systems and their spatial distribution within the supercluster can be clearly distinguished as shown in the right panel of Figure 4.

4.1.2 System mass uncertainties

Although Santiago-Bautista et al. (2020) did not provide uncertainties for the dynamical masses of their systems, we estimate such uncertainties for all SysCat systems, including both those identified by them from the SDSS galaxy sample and those identified by us from the 2dF and 6dF galaxy samples. The mass uncertainties were estimated here through simple error propagation (*i.e.*, $\Delta\gamma = [\sum(\Delta x_i \partial\gamma/\partial x_i)^2]^{1/2}$) such that, for each i-system

$$\Delta\mathcal{M}_{\mathrm{vir}_i} = \frac{\beta\pi}{2G}\sigma_{\upsilon_i}\sqrt{(2R_{\mathrm{vp}_i}\Delta\sigma_{\upsilon_i})^2 + (\sigma_{\upsilon_i}\Delta R_{\mathrm{vp}_i})^2}, \qquad (20)$$

where $\Delta\sigma_{\upsilon_i}$ represents the uncertainty in the system velocity dispersion, taken as $\sigma_{\upsilon_i}/\sqrt{N_i}$ (*e.g.*, Beers, Flynn, and Gebhardt 1990), and

$$\Delta R_{\mathrm{vp}_i} \approx \frac{2R^2_{\mathrm{vp}_i}}{N_i(N_i-1)} \times \frac{\Delta\theta(\bar{z}+1)}{D_{\mathrm{c}}(\bar{z})}\sqrt{\sum_{j<k}\left[\theta^{(i)}_{jk}\right]^{-6}}, \qquad (21)$$

is the propagated uncertainty in the projected mean radius of the system (at average redshift $\bar{z}$) due to the astrometric precision $\Delta\theta$ (in radians) of the galaxy angular position on the sky-plane (*e.g.*, $\Delta\theta \sim 0.1$ arsec for SDSS and $\Delta\theta \sim 0.2$ arcsec for 2dF and 6dF). Here, $\theta^{(i)}_{jk}$ represents the angular separation between pairs of observed member galaxies in the i-system.

The mass uncertainties with respect to redshift for the total sample of SysCat systems is shown in Figure 5. Note that there is no significant trend of the relative uncertainties (to increase or decrease) with respect to redshift. It can be seen that the uncertainties obtained are typical for this type of systems when compared with other catalogues: our relative uncertainties have mean and median values of 0.367 and 0.351, respectively (see the marginal histogram in the vertical axis of Fig. 5), similar to those obtained, for example, for the GalWCat19 (Abdullah et al. 2020), which have mean and median values of 0.372 and 0.343, respectively.

We have also compared the masses obtained by our method with those from other sources in the literature such as Top70 (Caretta et al. 2023; Zúñiga et al. 2024), which comprise 70 nearby well sampled galaxy clusters; GalWCat19 (Abdullah et al. 2020), a catalogue with 1,800 groups up to $z = 0.2$ from SDSS-DR13; and Tempel et al. (2014), a flux-limited catalogue of groups from SDSS-DR10, all considering only galaxies with spectroscopic redshifts. The comparison (Fig. 6) shows consistent mass estimates between the four samples and methods.

4.2 Detection of galaxy structures

The detection of structures inside superclusters of any redshift survey region (SDSS, 2dF or 6dF) was performed by an automated algorithm, similar to that of the detection of systems, but using the SysCat catalogues as input data. The procedure for each supercluster was:

(1) Using transformations from eq. (1), the member systems in the corresponding box were represented by the set $\mathcal{D} = \{(X_k, Y_k, Z_k),\ k = 1, ..., N_{\mathrm{sys}}\}$ of points, in rectangular coordinates, of their centroids compiled in SysCat. In this case, the set of points represents a three-dimensional space where the distances (in units of h^{-1}_{70} Mpc) can be calculated with the standard Euclidean metric.

(2) A DBSCAN-based algorithm, with input parameters $(\mathcal{D}, \varepsilon, 2)$, was applied for a range of neighborhood radii, $0 \leq \varepsilon \leq 25$ h^{-1}_{70} Mpc, to analyze the percolation properties of galaxy systems and determine the critical radius ε_c.

Figure 7 shows an example of PCs obtained for seven of the superclusters of Table 1 sampled in some of the surveys (SDSS, 2dF or 6dF). Again, the curves reach their maximum, *i.e.*, greatest number of detected 'clusters', when $\varepsilon = \varepsilon_c$. The value of ε_c obtained for each supercluster is shown in column 9 of Table 3. The variation of ε_c with respect to the mean redshift $\bar{z}$ of the supercluster, *i.e.*, the so-called percolation function (PF, *e.g.*, Chow-Martínez et al. 2014), can be seen in Figure 8. The critical radius that maximizes the detected amount of 'clusters' of galaxy systems in superclusters is, as expected, an increasing function of their mean redshift. For the total sample, ε_c has mean and median values of 10.4 h^{-1}_{70} Mpc and 9.6 h^{-1}_{70} Mpc, respectively.

(3) The radius ε_c was established as the most appropriate to find galaxy structures with $N_{\mathrm{min}} = 2$ in the supercluster box.

The number N_{str} of structures detected by the algorithm within each supecluster box is shown in column 10 of Table 3.

A total of 155 structures were identified in the full sample of superclusters. While in principle each SysCat-object represents a virialized –physical– galaxy system, the structures detected at this stage are only distance-linked 'clusters' of systems, but there is no guarantee that they are gravitationally bound structures or that they have enough density to survive the cosmic

https://doi.org/10.1017/pasa.2024.49 Published online by Cambridge University Press

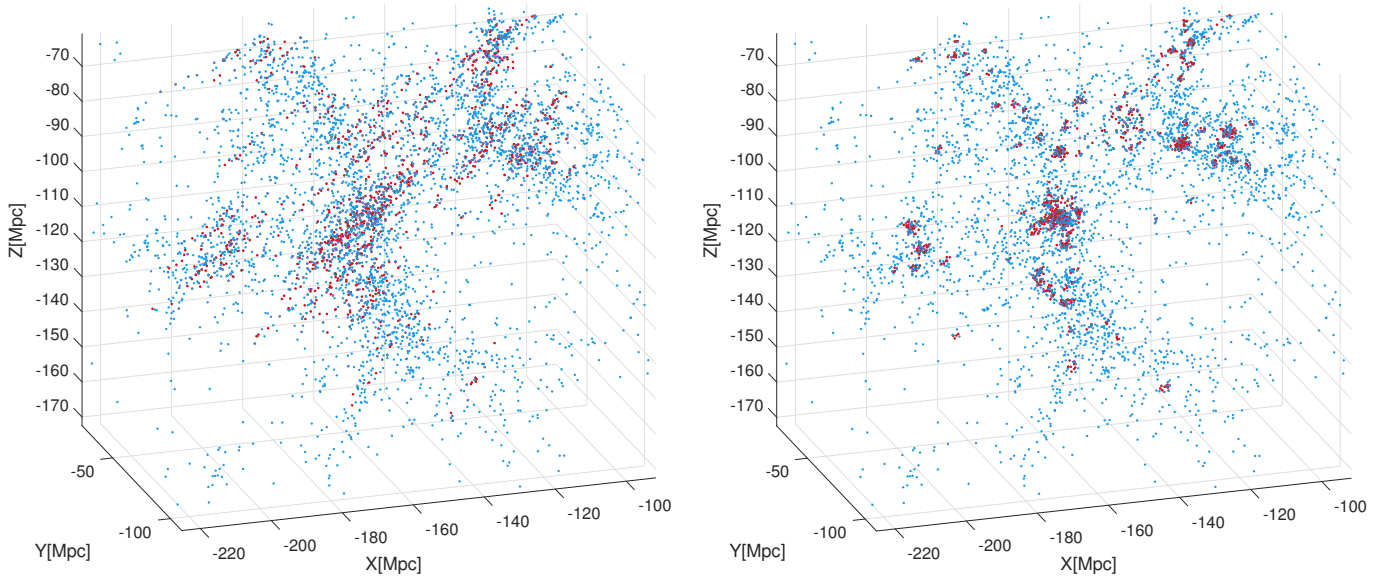

Figure 4. The initial supercluster box for the *Shapley Supercluster* (MSCC 389 and MSCC 401): each dot (4,649 in total) represents an observed 6dF galaxy in 3D-rectangular coordinates. On both panels the red dots represent the members of galaxy systems. *Left*: galaxy positions before the FoG-effect correction. *Right*: galaxy positions after FoG-effect correction.

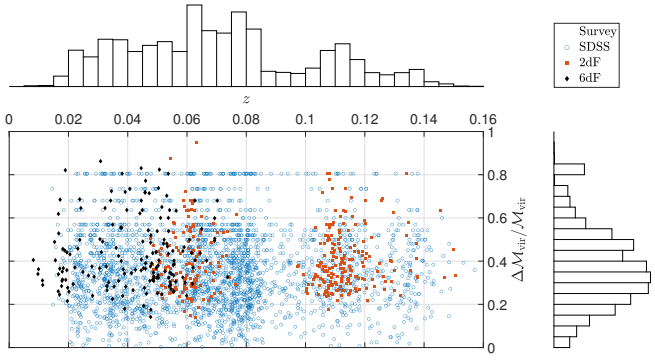

Figure 5. Distribution of relative mass uncertainties $\Delta\mathcal{M}_{\rm vir}/\mathcal{M}_{\rm vir}$ as a function of redshift for SysCat systems. The marginal histograms in the horizontal and vertical axes show the total distribution of systems (SDSS+2dF+6dF) with respect to redshift and relative mass uncertainties, respectively.

expansion. Several of the detected structures correspond to filaments, chains of galaxy systems that generally connected with each other if the neighborhood radius ε is allowed to grow as reported by J. Einasto et al. (1984). In what follows we will focus on selecting only those structures that meet the necessary criteria to be considered *cores* of superclusters.

4.2.1 *Extensive mass of structures*

The multiplicity m of each detected structure was defined as the number of systems (linked by DBSCAN) that compose it, and its *extensive mass*, *i.e.*, the sum[c] of the dynamical masses of its constituent parts, can be estimated in the form

$$\mathcal{M}_{\rm ext} = \sum_{i=1}^{m} \mathcal{M}_{{\rm vir}_k}, \tag{22}$$

where $M_{{\rm vir}_k}$ is the virial mass of each system in the structure. Assuming that all systems inside the structure are viralized, one might expect the total mass of a structure to be only slightly greater than its extensive mass, that is $\mathcal{M}_{\rm tot} \geq \mathcal{M}_{\rm ext}$. The difference in mass would be given by the matter (probably gas, galaxies or dark matter) that resides between systems or as a dispersed component, *i.e.*, not contained in galaxy systems.

In particular, the mass $\mathcal{M}^{\rm sc}_{\rm ext}$ of the superclusters was estimated from the above equation, but using $m = N_{\rm sys}$. The value of $\mathcal{M}^{\rm sc}_{\rm ext}$ (and its respective propagated uncertainty) for each supercluster in the sample is shown in column 5 of Table 3. For comparison, the masses of some well-known supercluster are available in the literature: the total mass of the *Coma-Leo* (MSCC 295) and *Hercules* (MSCC 474) superclusters are estimated in the ranges of $(168-189)\times10^{14}h_{70}^{-1}\mathcal{M}_\odot$ and $(67-260)\times10^{14}h_{70}^{-1}\mathcal{M}_\odot$, respectively (*e.g.*, Böhringer and Chon 2021); the mass of the *Shapley Supercluster* (MSCC 389 and MSCC 401) is estimated in the range of $(142-285)\times10^{14}h_{70}^{-1}\mathcal{M}_\odot$ (*e.g.*, Ragone et al. 2006; Sheth and Diaferio 2011); and the mass of the *Corona-Borealis Supercluster* (MSCC 463) lie in the range of $(67-420)\times10^{14}h_{70}^{-1}\mathcal{M}_\odot$ (*e.g.*, Small et al. 1998; M. Einasto et al. 2021). As can be seen, our estimates using

c. Note that this sum does not necessarily have to correspond to the value obtained, for example, by applying the virial mass equation (15) to the sample of member galaxies of the structure. The calculation of virial mass can be under or over estimated due to the presence of substructures (*e.g.*, Biviano et al. 2006), such as the member systems of a structure, so it is not an extensive parameter. The term 'extensive' here is used because of the additive property of mass.

https://doi.org/10.1017/pasa.2024.49 Published online by Cambridge University Press

Table 3. General properties of the MSCC-superclusters in the sample

ID MSCC (1)	RA_{CM} [deg] (2)	Dec_{CM} [deg] (3)	z_{CM} [deg] (4)	$\mathcal{M}^{sc}_{ext}$ $[10^{14} h_{70}^{-1} \mathcal{M}_\odot]$ (5)	V_{sc} $[10^3\ h_{70}^{-3}\ Mpc^3]$ (6)	$\rho_{sc} = \mathcal{M}^{sc}_{ext}/V_{sc}$ $[10^{10} h_{70}^{2} \mathcal{M}_\odot Mpc^{-3}]$ (7)	$n_{sc} = N_{gsc}/V_{sc}$ $[h_{70}^{3}\ Mpc^{-3}]$ (8)	ε_c $[h_{70}^{-1}\ Mpc]$ (9)	N_{str} (10)	N_{crs} (11)
1	0.32	-29.24	0.061	143.24 ± 7.38	150.4	9.5 ± 0.4	0.0391	5.3	4	3
27	9.61	-26.97	0.062	19.59 ± 1.67	73.8	2.6 ± 0.2	0.0312	5.7	1	1
33	10.68	-29.85	0.110	201.42 ± 9.14	268.3	7.5 ± 0.3	0.0236	8.3	5	5
39	13.18	-11.12	0.054	41.84 ± 5.45	57.0	7.3 ± 0.9	0.0129	6.0	2	2
55	18.03	15.56	0.060	32.53 ± 5.95	24.7	13.1 ± 2.4	0.0210	7.1	2	1
72	25.13	0.00	0.080	66.25 ± 6.13	60.5	10.9 ± 1.0	0.0276	8.0	4	2
75	27.93	-1.04	0.086	72.06 ± 8.94	100.0	7.2 ± 0.8	0.0118	14.0	2	0
76	29.17	-1.64	0.123	59.68 ± 7.95	450.6	1.3 ± 0.1	0.0043	12.4	2	0
117	51.57	-47.59	0.061	91.11 ± 11.16	129.3	7.0 ± 0.8	0.0111	6.1	1	1
175	125.13	18.78	0.094	65.23 ± 5.59	122.5	5.3 ± 0.4	0.0153	14.0	3	1
184	130.06	29.95	0.103	37.19 ± 4.40	204.1	1.8 ± 0.2	0.0071	9.4	2	1
211	149.10	64.08	0.118	7.44 ± 3.01	27.6	2.6 ± 1.0	0.0223	12.7	1	0
219	153.45	19.20	0.114	77.87 ± 8.45	257.6	3.0 ± 0.3	0.0063	10.6	1	1
222	156.66	50.04	0.138	47.46 ± 6.98	107.8	4.4 ± 0.6	0.0104	13.6	2	2
223	153.74	62.78	0.138	7.23 ± 4.42	12.9	5.6 ± 3.4	0.0172	12.0	1	0
229	157.19	34.24	0.136	30.21 ± 6.21	368.0	0.8 ± 0.1	0.0035	13.2	1	0
236	160.88	16.12	0.032	155.02 ± 10.78	158.6	9.7 ± 0.6	0.0459	8.8	5	4
238	158.64	38.40	0.105	177.01 ± 14.26	1412.2	1.2 ± 0.1	0.0048	7.8	10	4
248	159.07	44.66	0.125	16.37 ± 2.70	197.8	0.8 ± 0.1	0.0041	35.0	1	0
264	167.30	12.29	0.117	16.77 ± 7.14	202.4	0.8 ± 0.3	0.0065	9.8	1	0
266	166.28	12.28	0.126	43.29 ± 7.83	29.5	14.6 ± 2.6	0.0169	12.0	1	1
272	167.54	40.96	0.075	23.93 ± 2.22	36.3	6.5 ± 0.6	0.0309	8.0	1	1
277	169.47	50.11	0.109	103.33 ± 10.20	103.8	9.9 ± 0.9	0.0169	8.2	2	3
278	171.27	25.17	0.031	107.07 ± 4.62	268.7	3.9 ± 0.1	0.0274	8.0	4	3
283	171.76	20.82	0.134	80.42 ± 9.08	290.3	2.7 ± 0.3	0.0051	16.5	4	3
295	183.39	22.27	0.022	159.78 ± 6.83	153.8	10.3 ± 0.4	0.0791	6.0	2	2
310	173.20	54.32	0.060	251.39 ± 9.50	351.5	7.1 ± 0.2	0.0290	8.0	6	5
311	174.51	11.89	0.083	142.23 ± 7.78	294.4	4.8 ± 0.2	0.0154	8.6	3	3
314	177.19	-1.73	0.079	26.85 ± 4.32	3.4	78.5 ± 12.6	0.1184	7.4	1	1
317	177.01	-1.59	0.124	48.89 ± 7.14	77.2	6.3 ± 0.9	0.0085	6.8	2	2
323	179.79	26.05	0.138	106.49 ± 11.73	174.0	6.1 ± 0.6	0.0098	16.2	3	3
333	181.55	30.27	0.079	33.33 ± 5.05	12.8	25.9 ± 3.9	0.0829	9.5	2	2
335	181.74	29.43	0.073	55.74 ± 7.83	57.8	9.6 ± 1.3	0.0369	9.9	5	1
343	182.05	12.66	0.082	66.17 ± 5.16	21.8	30.3 ± 2.3	0.0781	10.0	5	4
360	190.45	63.67	0.105	39.88 ± 4.65	299.3	1.3 ± 0.1	0.0064	10.0	2	1
386	198.67	39.60	0.069	77.39 ± 5.58	146.9	5.2 ± 0.3	0.0181	9.0	3	2
389	201.48	-31.99	0.046	171.33 ± 9.01	191.0	8.9 ± 0.4	0.0198	6.0	6	3
407	208.70	25.63	0.136	12.81 ± 2.19	92.1	1.3 ± 0.2	0.0068	15.1	1	0
414	212.27	26.76	0.067	298.68 ± 11.43	242.0	12.3 ± 0.4	0.0372	8.5	7	5
419	212.98	7.18	0.112	96.06 ± 9.39	70.5	13.6 ± 1.3	0.0189	11.0	3	3
422	210.19	26.78	0.139	7.35 ± 1.79	199.9	0.3 ± 0.0	0.0041	12.6	1	0
430	218.56	24.33	0.095	48.33 ± 4.67	95.3	5.0 ± 0.4	0.0136	9.6	4	2
440	223.15	21.55	0.115	83.57 ± 7.21	244.3	3.4 ± 0.2	0.0107	12.0	2	1
441	223.96	28.02	0.125	15.35 ± 3.73	130.7	1.1 ± 0.2	0.0049	15.0	1	1
454	228.78	6.96	0.044	172.79 ± 8.04	249.3	6.9 ± 0.3	0.0224	7.5	5	4
457	229.57	5.64	0.079	173.07 ± 9.61	177.1	9.7 ± 0.5	0.0215	9.8	4	4
460	229.89	31.06	0.114	169.83 ± 11.18	163.9	10.3 ± 0.6	0.0158	10.9	4	3
463	232.79	29.37	0.073	312.36 ± 13.20	326.1	9.5 ± 0.4	0.0218	9.0	6	5
474	239.46	15.69	0.036	120.34 ± 4.98	64.2	18.7 ± 0.7	0.1030	9.6	5	3
484	246.08	41.86	0.134	24.74 ± 4.35	4.4	56.3 ± 9.9	0.0550	13.6	1	1
509	310.21	-40.02	0.020	39.05 ± 3.24	176.9	2.2 ± 0.1	0.0146	5.2	3	2
574	349.03	-26.76	0.119	104.17 ± 7.94	412.6	2.5 ± 0.1	0.0097	10.0	3	2
579	353.89	9.97	0.040	24.52 ± 2.77	121.2	2.0 ± 0.2	0.0098	9.0	2	1

https://doi.org/10.1017/pasa.2024.49 Published online by Cambridge University Press

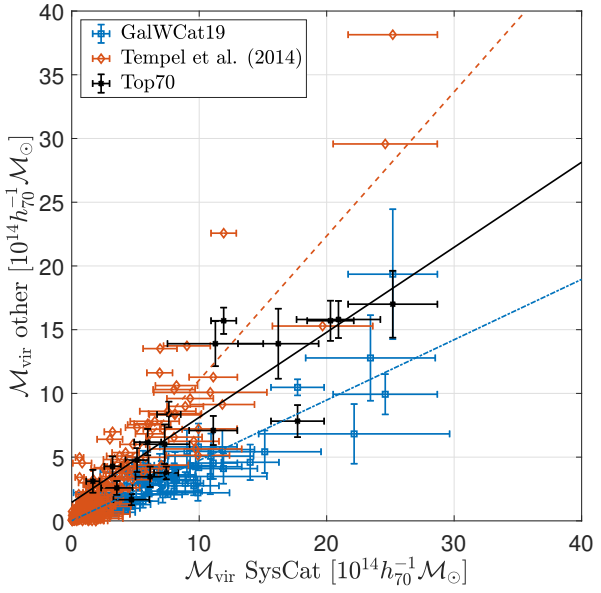

Figure 6. Comparison of SysCat masses with system masses from other similar catalogues: GalWCat19 (Abdullah et al. 2020) masses are $\mathcal{M}_{100}$ calculated from a NFW profile, the ones closest to $\mathcal{M}_{\rm vir}$; Tempel et al. (2014) are total masses estimated assuming a Herniquist density profile; and Top70 (Caretta et al. 2023; Zúñiga et al. 2024) are also virial masses, estimated in a similar way but with a different (and more complete) database. SysCat and Tempel groups tend to slightly overestimate the masses with respect to Top70, while GalWCat19 slightly underestimates them

$\mathcal{M}_{\rm ext}^{\rm sc}$ are consistent with the mass ranges determined by other authors.

4.2.2 *Volume estimations*

The volume of any structure can be approximated by the volume enclosed by the surface enclosing its member galaxies (represented as points in FoG-corrected rectangular coordinates from eq. (1)). Such enclosing surfaces can be built by triangulating boundary points using alpha-shape based algorithms (*e.g.*, Edelsbrunner and Mücke 1994) that allow polyhedral surfaces to be built around sets of points in three-dimensional space.

In particular, in this work a MATLAB alpha-shape based algorithm (see MATLAB 2023) was used, which allows the generation of a single polyhedral surface around a set of points (x, y, z) in three-dimensional space and returns an estimate of the volume enclosed by it. In such algorithm the fit of polyhedral surfaces can be adjusted (tightened/loosened) by means of a 'shrink factor' $s_{\rm f}$ ranging from 0, generating the convex hull, to 1, generating the compact boundary. Figure 9 shows the polyhedral surface fit, with $s_{\rm f}$ = 1, made for the *Shapley Supercluster* from the galaxies contained in its –FoG-corrected and purified– supercluster box. The volumes $V_{\rm sc}$ of the sampled superclusters are shown in column 6 of Table 3. Such values were estimated by fitting polyhedral surfaces, with $s_{\rm f}$ = 1, to the set of member galaxies in each refined supercluster box.

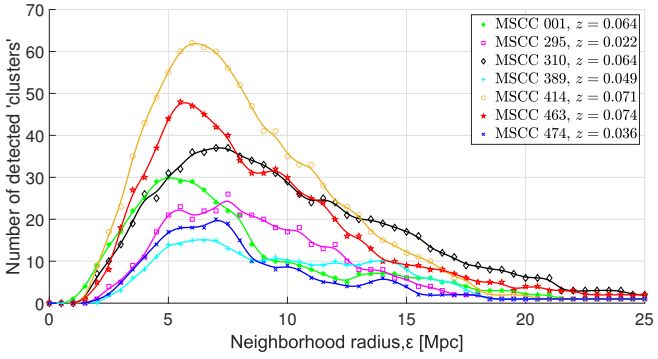

Figure 7. Percolation curves (PCs) obtained for seven of the superclusters in the sample, using galaxy systems as input data. The PCs show the variation in the number of second-order galaxy 'clusters', *i.e.*, 'clusters' of galaxy systems with $N_{\rm min}$ = 2, detected by the DBSCAN algorithm as the neighborhood radius varies. The lines represent the smoothing-spline of data and their maxima are located at the critical neighborhood radius, ε_c.

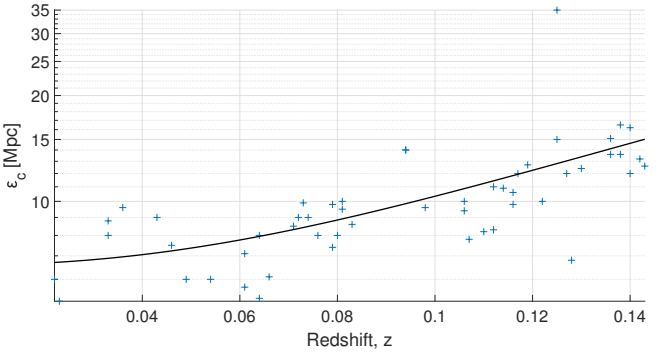

Figure 8. Percolation function (PF) obtained for the supercluster sample: critical neighborhood radius for detecting galaxy structures increases as a function of supercluster redshift. The solid black line represents the best fit (goodness, $\mathcal{R}^2_{\rm det}$ = 0.34) to the data: a power law $az^b + c$ with coefficients a = 685.20, b = 2.26 and c = 6.58. In general, the critical radius used to detect galaxy structures increases with mean redshift due to incompleteness and thus the loss of galaxy density.

5. Identification of supercluster *cores*

5.1 *Purifying the galaxy sample in superclusters*

To identify *cores*, we first refined the samples of supercluster 'member' galaxies from both southern and SDSS samples as follows:

(1) Inside each supercluster box, a FoF algorithm was applied to the set of $N_{\rm sys}$ systems identified there to determine the smallest radius $\varepsilon_{\rm sc}$ linking them all. For this, each (SysCat) system was visualized as a single point, its centroid (c_i) in rectangular coordinates.

(2) For each galaxy (g_*) in the corresponding initial FoG-corrected supercluster box $(\mathcal{B}_{\rm sc})$, its Euclidean distance $d(g_*, c_i)$ to each galaxy system was calculated. Galaxies were provisionally labeled as 'linked' to the nearest galaxy system.

(3) All galaxies within a radius $\varepsilon_{\rm sc}$ around the centroid of the system to which they were 'linked' were taken as a

https://doi.org/10.1017/pasa.2024.49 Published online by Cambridge University Press

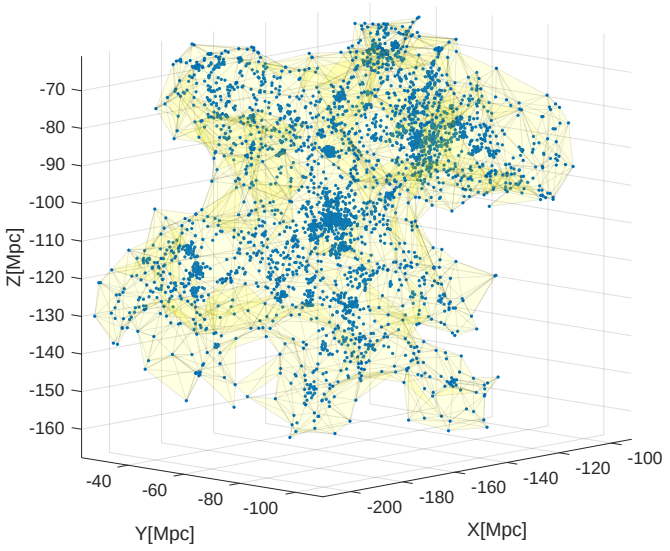

Figure 9. Polyhedral surface (compact boundary, with shrink factor $s_f = 1$) fitted to the —purgued and FoG-corrected— sample of member galaxies of *Shapley Supercluster* (MSCC 389 and MSCC 401). The volume enclosed by the compact boundary is $V_{sc} = 191.1\ h_{70}^{-3}$ Mpc^3, smaller than that which would enclosed by the convex hull (*e.g.*, with $s_f = 0$) since the latter include voids of considerable size.

'member' of the respective supercluster. The final, purified, supercluster box ($\mathcal{G}_{sc}$) only contains the galaxies selected as 'members'. This set of 'member' galaxies can be represented, for each supercluster, in the form

$$\mathcal{G}_{sc} = \left\{ g_* \in \mathcal{B}_{sc} | \min_i \{ d(g_*, c_i) \} \leq \varepsilon_{sc}, i = 1, ..., N_{sys} \right\}. \quad (23)$$

Galaxies not selected by this criterion were considered as 'field' galaxies, not belonging to superclusters. There is no univocal criterion to define the membership of a galaxy to a supercluster, so here the criterion was to include all galaxies that are members of systems as well as those that are between them, forming galaxy bridges or being part of the disperse component of the supercluster up to a distance that we consider reasonable, *e.g.*, ε_{sc} from each identified galaxy system.

The radius ε_{sc} and the number $N_{g_{sc}}$ of 'member' galaxies found for each supercluster are shown respectively in columns 10 and 11 of Table 1.

5.2 *Definition of* cores

Rich superclusters have central regions of high density of galaxies (and systems) that are absent in poor superclusters (*e.g.*, Einasto, Einasto, Tago, Saar, Liivamägi, et al. 2007; M. Einasto et al. 2008). Such regions, commonly called *cores*, may be observationally defined as collections of rich (and poor) clusters, groups and individual galaxies, being identified by their high galaxy density contrasts ($\delta > 10$, according to Einasto, Einasto, Tago, Saar, Liivamägi, et al. 2007; M. Einasto et al. 2021). Given these characteristics, it could be said that *cores* are "internal structures of superclusters that have begun to materialize as recognizable entities" (*e.g.*, Araya-Melo et al. 2009), like 'compact superclusters' (*e.g.*, Pearson, Batiste, and Batuski 2014). The most important characteristic of these entities is probably that they are the largest structures in the Universe that are expected to survive cosmic expansion, reaching, at least marginally, dynamical equilibrium.

In this work only rich MSCC-superclusters (with $m \geq 5$ member Abell/ACO-clusters) have been selected, so the presence of *cores* is expected in them. To identify the *cores* we think of them as *massive and gravitationally bound galaxy structures, within superclusters, comprised of two or more galaxy systems (groups or clusters), with high probability of future collapse and virialization*. The *cores* of superclusters involve high local densities in regions of small volume (*i.e.*, Marini et al. 2004). Based on the above, we choose as *core* candidates those structures that, at the present-epoch, meet the following conditions:

i. Have extensive masses $\mathcal{M}_{ext} \geq 5 \times 10^{14} h_{70}^{-1} \mathcal{M}_\odot$.
ii. Are composed by gravitationally bound galaxy systems.
iii. Have a density ratio $\mathcal{R} \geq 7.86$ and an overdensity $\Delta_{cr} \geq 1.36$.

The first condition allows the massive systems to be used as markers (or "seed" points, *e.g.*, Chow-Martínez 2019) of *cores*; rich galaxy clusters, for example, are powerful indicators of local density in supercluster environments (M. Einasto et al. 2008). The minimum mass $5 \times 10^{14} h_{70}^{-1} \mathcal{M}_\odot$ (*e.g.*, $\sim 10^{15} h_{70}^{-1} \mathcal{M}_\odot$ chosen by Araya-Melo et al. (2009) to select bound superclusters in cosmological simulations) is of the order of magnitude of the richest clusters, so any mass above that represents a considerable galaxy agglomeration. Thus, searching for systems with large virial masses increases the probability of finding nucleation regions, *i.e.*, zones of higher concentration of matter in the form of clusters, groups, individual galaxies and hot gas.

The spherical density criterion described in Section 3.3 forms a key ingredient in our definition of *cores* and for their selection process from the identified structures. Conditions (ii) and (iii) above, together, guarantee, at least theoretically, that galaxy structures once gravitationally bound will begin to collapse to virialize in the future according to the threshold values presented in Table 2. In fact, condition (iii) could guarantee, by itself, that the structures under these density conditions will remain bound despite the expansion. However, an alternative method is used here to analyze the current gravitational binding state of the structures, which is why the second condition is taken independently.

5.3 *Core selection*

Using the three conditions stated above to define *cores*, these were selected from among the structures identified within each supercluster in the sample. The selection process was developed through a semi-automatic analysis as follows:

https://doi.org/10.1017/pasa.2024.49 Published online by Cambridge University Press

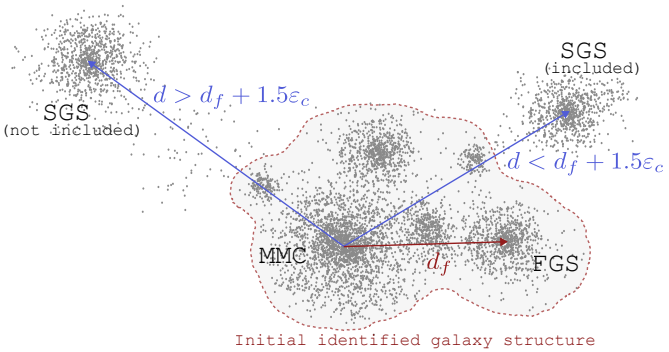

Figure 10. Schematic of a galaxy structure identified by DBSCAN with a critical neighborhood radius ε_c. Its initial member systems are enclosed by the red dashed line, and d_f is the distance between the Most Massive Cluster (MMC) and the Farthest Galaxy System (FGS) from it inside the structure. The systems outside the dashed line (if they exist) are called Surrounding Galaxy Systems (SGS). If any SGS is found in the spherical shell of radii d_f and $d_f + 1.5\varepsilon_c$, centered on the MCC, it is provisionally taken as a member of the structure. Whether or not a member system remains in the structure will depend on the gravitational binding criteria.

(1) The extensive mass of each structure is calculated by eq. (22) and used as an approximation for its total mass. Only structures with $\mathcal{M}_{\rm ext} \geq 5 \times 10^{14}\ h_{70}^{-1}\mathcal{M}_\odot$ are accepted as *core* candidates.

(2) For each structure, its Most Massive Cluster (MMC), *i.e.*, the member galaxy system with the largest virial mass, is identified and the distance d_f from this to the farthest constituent system of the initial structure is determined. Then, all the systems in the surroundings of the structure (if any in the supercluster box), within the spherical shell between d_f and $d_f + 1.5\varepsilon_c$, centered on the MMC centroid, are provisionally included as members of the –enlarged– structure (see Figure 10). Here, ε_c is the corresponding critical neighborhood radius used to identify the initial structure (see column 7 of Table 3). Here, a new $\mathcal{M}_{\rm ext}$ for the enlarged structure is calculated if it is the case.

(3) The state of gravitational binding between pairs of member systems inside the enlarged structure is analyzed using the criterion established in eq. (7): a member is classified as *directly-bound* ($\mathcal{D}_b$-member) if it meets the criterion paired with the MMC or as *indirectly-bound* ($\mathcal{I}_b$-member) if it does not meet the criterion with the MMC, but is linked to a third member that is directly-bound to both separately (like a 'gravitational FoF'). These two sets of members form, together with the MMC, the *pairwise bound region* of the structure. Members of the enlarged structure that are neither *directly-* nor *indirectly-bound* to the MMC are classified as *possibly-bound* ($\mathcal{P}_b$-member). This can happen because these $\mathcal{P}_b$-members can still be bound to the larger mass of the whole structure, even if not bound to a specific neighbor.

(4) In a complementary way, the gravitational binding state of the structure as a whole is analyzed using the criterion established in eq. (11). For this, the line-of-sight velocity dispersion $\sigma_{\upsilon_{\rm sys}}$ of systems inside the structure is estimated from their mean velocities using Tukey's biweight robust method (*e.g.*, Beers, Flynn, and Gebhardt 1990), which is best suited for the small amount of member radial velocity data, and $\beta = 2.5$, taken assuming a weak anisotropy in the velocity distribution of member systems. Furthermore, in order to estimate the gravitational radius r_G, the virial mass $\mathcal{M}_{{\rm vir}_k}$ of each member system of the structure is used in eq. (10).

(5) If the structure contains a pairwise bound region and $\mathcal{P}_b$-members, then one of the following two cases could occur:

(a) If the structure is bound as a whole (or globally bound), then the $\mathcal{P}_b$-members are considered as bound members and the entire enlarged structure is accepted.

(b) Instead, if the structure is not globally bound, the farthest $\mathcal{P}_b$-member from the MMC is removed and step (4) is performed again. The process is repeated until a globally bound structure is obtained, stripped of unbound members, or until only the pairwise bound region remains.

On the other hand, cases may occur in which there are no pairwise bound systems within a structure (*i.e.*, there is no a pairwise bound region), but it is globally bound. These type of structures are also accepted.

In any case, the structures accepted after this step continue to be considered *core*-candidates of the corresponding supercluster, while the others are discarded.

(6) The member galaxies of each *core*-candidate are defined as all galaxies up to a distance of $3.5R_{{\rm vir}_k}$ from the centroid of each k-th member system in the corresponding FoG-corrected supercluster box. At the chosen distance we expect to select the galaxies of member systems up to about their turn-around zone, those present in bridges between them, as well as galaxies that can be considered as the disperse component of the *core*-candidate. The photometric and spectroscopic data of *core* galaxies are extracted from the respective GalCat catalogue.

(7) The mean densities of each *core*-candidate and its corresponding host supercluster are estimated, respectively, in the form

$$\rho_{\rm c} = \frac{\mathcal{M}^{c}_{\rm ext}}{V_{\rm c}}, \quad \text{and} \quad \rho_{\rm sc} = \frac{\mathcal{M}^{\rm sc}_{\rm ext}}{V_{\rm sc}}, \tag{24}$$

where $\mathcal{M}^{c}_{\rm ext}$ and $\mathcal{M}^{\rm sc}_{\rm ext}$ are the extensive masses of the *core*-candidate and the supercluster, and $V_{\rm c}$ and $V_{\rm sc}$ are the respective volumes estimated from the spatial distribution of their member galaxies using the alpha-shape based method described in Section 4.2.2, with $s_{\rm f} = 0.5$ for *core*-candidates and $s_{\rm f} = 1$ for superclusters. The reason for this choice of shrink factors is explained below.

https://doi.org/10.1017/pasa.2024.49 Published online by Cambridge University Press

The masses $\mathcal{M}_{\rm ext}^{\rm sc}$ and volumes $V_{\rm sc}$ used here for superclusters are those compiled in columns 5 and 6 of Table 3, while the respective (mass and galaxy) densities calculated from these values are shown in columns 7 and 8 of the same table. The estimated gravitational radius, extensive mass, volume and density values for the *core*-candidates are presented in Table 5 only for those that were finally selected as *cores* (see Section 6).

Now, assuming $\rho_{\rm sc}$ to be the local background density of each *core*-candidate in its respective supercluster, its density ratio is calculated from eq. (12) in the form

$$\mathcal{R} = \frac{\rho_{\rm c}}{\rho_{\rm sc}}, \tag{25}$$

and its density contrast with respect to the critical density from eq. (13) as

$$\Delta_{\rm cr} = \frac{8\pi G\rho_{\rm c}}{3H^2(z)} - 1 \tag{26}$$

where z is the mean redshift of the host supercluster using the cosmology parameters described in Section 1. Finally, only candidates that meet criteria $\mathcal{R} \geq 7.86$ and $\Delta_{\rm cr} \geq 1.36$ (see Table 2) are considered *cores*, and the other structures were rejected.

We took the values $s_{\rm f} = 0.5$ and $s_{\rm f} = 1$, respectively, for the polyhedral fit shrink factors of the *core*-candidates and superclusters, because with these values we have the worst case scenario for the density ratio (contrast) of a *core*-candidate, possibly underestimating its density and overestimating the density of its local environment (the host supercluster). If a candidate meets the criteria under these conditions, they will meet the criteria under any other volume setting. A summary of the *core* selection process (or CorSel Algorithm) is shown in Figure 11.

The top panel of Figure 12 shows an example of the *cores* identified in the *Shapley Supercluster* labeled with the respective main Abell/ACO-clusters that constitute them. The polyhedral surfaces fitted (with $s_{\rm f} = 0.5$) to the member galaxies of the *core*, and used to determine the volumes of these, are also shown. The bottom panel of Figure 12 shows in greater detail the distribution of member galaxies in the so called main *core* (*i.e.*, A3556-A3558-A3562 and other clusters) of *Shapley Supercluster* and the Abell/ACO-clusters that match its member systems. The three *cores* identified for the *Shapley Supercluster* also correspond to the regions with high surface density of galaxies in the RA-Dec plane, as can be seen in Figure 13. Note that there is a forth surface overdensity in this figure, north of the main *core*, corresponding to the region of A1736 cluster: this region do not correspond to a *core* because the overdensity is caused by a projection effect (A1736 is composed of two rich systems aligned towards the LOS, *e.g.*, Caretta et al. 2023). These cases can be identified in all superclusters that have *cores* in our sample.

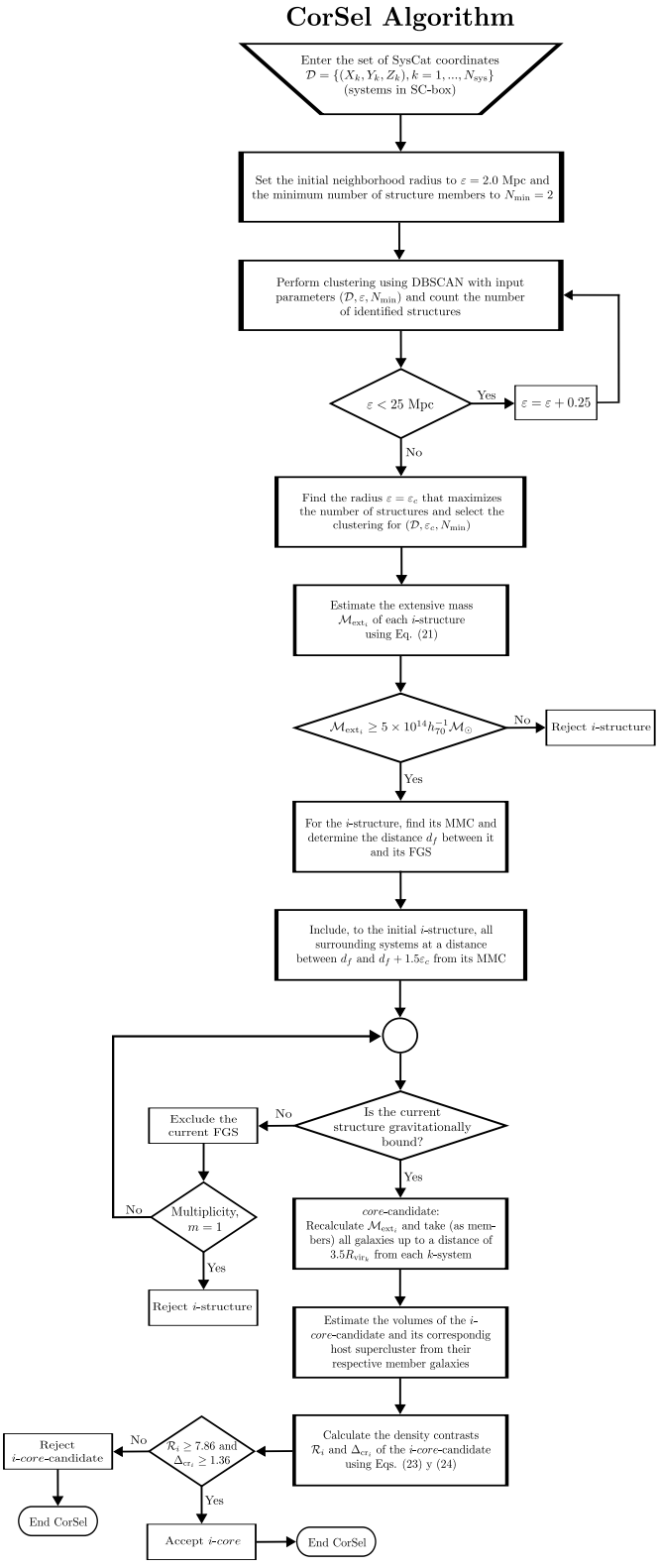

Figure 11. Flow chart of the semi-automatic CorSel-Algorithm.

The number of *cores* ($N_{\rm crs}$) found within each supercluster box, following the steps and criteria described above, is shown in column 11 of Table 3. From the histogram in the top panel of Figure 14 it can be noted that about 83% of the MSCC

https://doi.org/10.1017/pasa.2024.49 Published online by Cambridge University Press

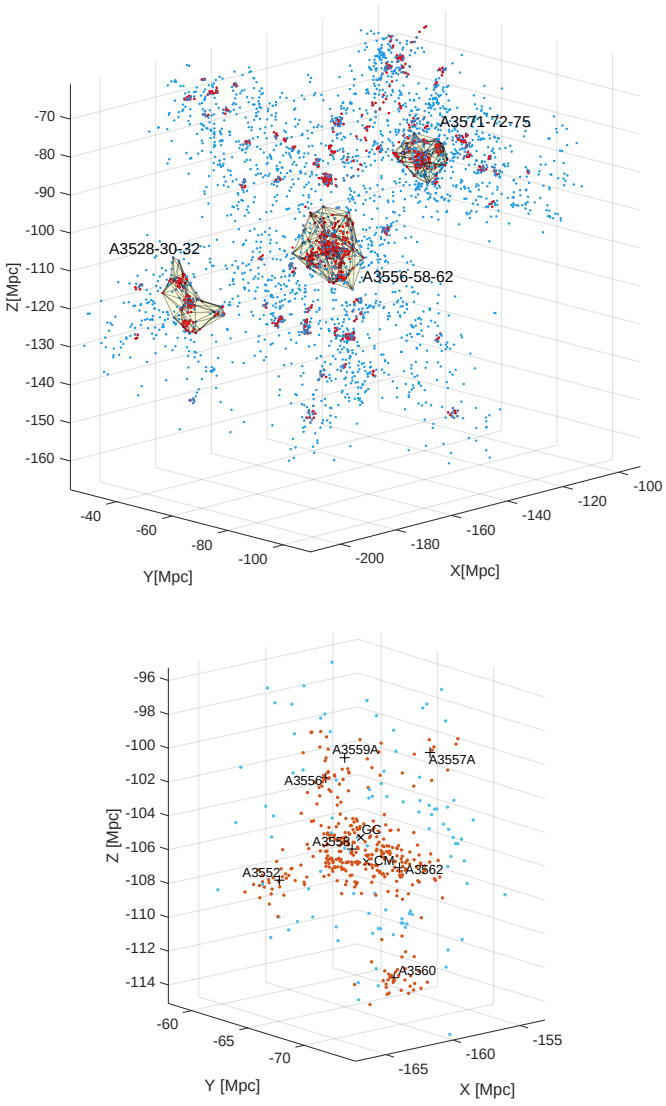

Figure 12. *Top*: The three *cores* identified for the *Shapley Supercluster* (MSCC 389 and MSCC 401). The red points enclosed by yellow polyhedral surfaces correspond to the member galaxies of the systems of the respective *cores*. The labels in each *core* inform about the main Abell/ACO-clusters that comprise them. *Bottom:* the main *core* of the *Shapley Supercluster* with 448 member 6dF-galaxies. The red dots represent the member galaxies of systems (Abell/ACO-clusters in this case), while the blue dots represent galaxies in bridges and disperse component; CM and GC are respectively the center of mass and the geometric center (centroid) of the *core*; the black '+' symbols represent the centroids of the member clusters from the Abell/ACO catalogue.

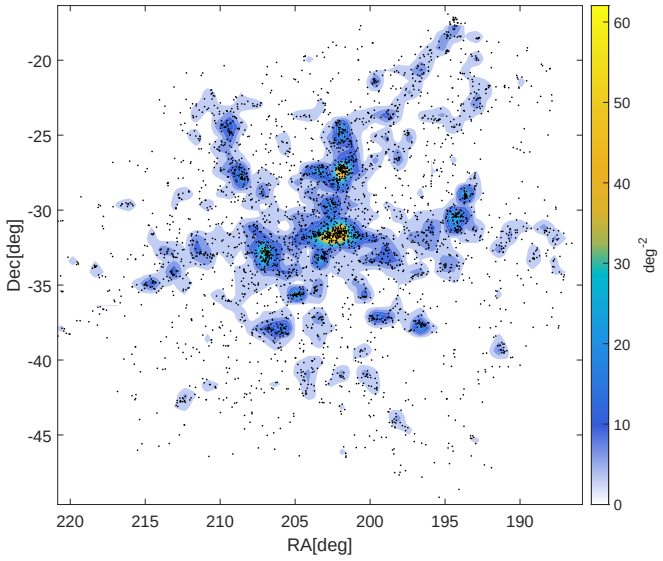

Figure 13. 2-D surface density map of the RA-Dec distribution of galaxies in the *Shapley Supercluster* (MSCC 389 and MSCC 401). Three of the regions with the highest density of galaxies correspond to the *cores* identified for the *Shapley Supercluster*: DCC 066 (RA = 194.211, Dec = –30.698), DCC 067 (RA = 202.604, Dec = –31.075) and DCC 068 (RA = 207.434, Dec = –32.631). The density peaks correspond to the most massive clusters of each *core*.

rich superclusters in the sample have at least one *core*, about 19% have two *cores*, and about 36% have three or more *cores*. Additionally, the boxplot in the bottom panel of Figure 14 shows a clear correlation between the number of *cores* and the extensive mass (*e.g.*, $\mathcal{M}^{\rm sc}_{\rm ext}$ in Table 3) of their host superclusters. This correlation is expected given that the more massive a supercluster is, the greater the probability of forming regions (internal structures) with sufficient density to bind gravitationally and break away from the cosmic expansion. The sampled MSCC-superclusters with masses below $\sim 10^{15} h_{70}^{-1} \mathcal{M}_\odot$ tend to have fewer than three *cores*, while those with masses above that value tend to have three or more.

6. The DCC *core*-catalogue

All the galaxy structures accepted as *cores* were included in what we have called the Density-based *Core* Catalogue (DCC). This catalogue contains a total of 105 massive nucleation regions inside nearby rich superclusters and with a high probability of future collapse and virialization, that are expected to survive the cosmic expansion to become "island universes" (*e.g.*, Dünner et al. 2006). To complement our previous definition, *cores* are considered here as compact superclusters, *i.e.*, dense ($\mathcal{R} \geq 7.86$ and $\Delta_{\rm cr} \geq 1.36$) and probably gravitationally bound structures, formed by two or more galaxy systems of which at least one must be a rich and massive galaxy cluster (the "seed" cluster) of the Local Universe.

In Table 4 we list information on the 105 structures identified as *cores* in the sample of 53 rich superclusters with redshift between 0 and ∼0.15: column 1 lists the number of the DCC and column 2 the number of the MSCC-supercluster it belongs to; the triplets of columns 3 to 5, 6 to 8 and 9 to 11 show the RA, Dec and z values for the *core* geometric centers (centroids), the centers of mass of the *cores* and the centroid of the MMC associated with each *core*, respectively; columns 12 and 13 present, respectively, the number of galaxies $N_{\rm g}$ and the number m_c (multiplicity) of galaxy systems identified for the *cores*; finally, column 14 shows some matches between the *core* member systems and the Abell/ACO clusters (including the S-clusters, *e.g.*, Abell, Corwin, and Olowin 1989) as well as

https://doi.org/10.1017/pasa.2024.49 Published online by Cambridge University Press

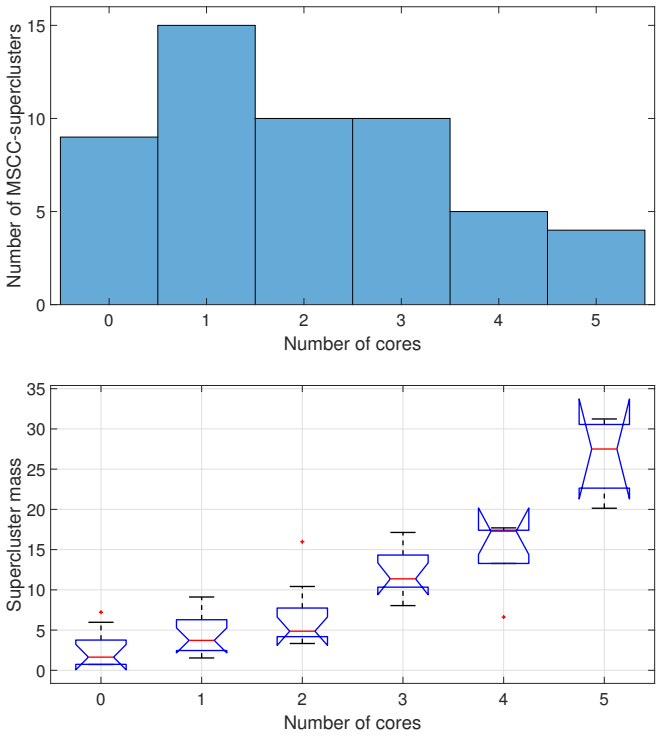

Figure 14. *Top*: The histogram shows the number of superclusters as function of the number of *cores* they contain. *Bottom*: Box plot showing the relationship between the extensive mass of superclusters ($\mathcal{M}_{\rm ext}^{\rm sc}$ in units of $10^{14}h_{70}^{-1}\mathcal{M}_{\odot}$) and the number of *cores* they contain; the boxes represent the interquartile range with the red line indicating the median mass, the whiskers add 1.5 times the interquartile range, and notches display the confidence interval (with a significance level of 0.05) around the median.

with clusters and groups from other catalogues mentioned in the table notes. This was performed in NED[d], taking matches within a radius of 5 arcmin around the position of each *core* system and with a radial velocity tolerance of ±200 km/s in LOS (when available). Column 14 is separated into two sub-columns which show the best matches (if any) for the MMC (left) and the other member systems (right) of each *core*.

With the exception of a few structures for which a warning will be issued later, most DCC-*cores* meet both the gravitational binding and density criteria required for their selection in the considered redshift range. Furthermore, some structures with extensive masses below $5\times10^{14}\ h_{70}^{-1}\mathcal{M}_{\odot}$ were included in the DCC catalogue because, despite their relatively low mass, they meet all other criteria established for selecting *cores*. In Table 5 we compile some additional properties estimated for the detected DCCs: column 1 shows the ID of the *core* in the DCC catalogue; column 2 presents the line-of-sight velocity dispersion $\sigma_{\upsilon_{\rm sys}}$ of member galaxy systems inside the *core*; column 3 shows the extensive mass $\mathcal{M}_{\rm ext}^{c}$ of the *core*; column 4 contains the gravitational radius of the *core*; column 5 presents the volume of the *core* estimated by the polyhedral fit method, with $s_{\rm f}$ = 0.5, from its FoG-corrected member galaxies; columns 6 and 7 show, respectively, the mass density and number density of galaxies of the *core*; column 8 presents the galaxy number density contrast of the *core* with respect to its respective host supercluster, $\delta_{\rm g}^{c} = n_c/n_{\rm sc} - 1$; columns 9 and 10 show, respectively, the density ratio $\mathcal{R}$ (with respect to the local mass density) and the density contrast $\Delta_{\rm cr}$ (with respect to the critical density at redshift z) of the *core*, with their respective uncertainties propagated through the calculations; column 11 shows the gravitational binding state of the *core* as a whole (*i.e.*, using criterion (11)); and, finally, column 12 shows the 3-D distance $d_{\rm CMs}$ between the center of mass of the *core* and the center of mass of its respective host supercluster.

Note that the structures DCC 013, DCC 061, DCC 101 and DCC 102 have extensive masses less than $5\times10^{14}h_{70}^{-1}\mathcal{M}_{\odot}$, the threshold mass established in the *core* definition criteria of Section 5.2, however they are gravitationally bounded structures and their density contrasts $\mathcal{R}$ and $\Delta_{\rm cr}$ are higher than the thresholds necessary to guarantee future collapse and virialization, which is why they were included in the DCC catalogue. On the other hand, the structures DCC 016, DCC 019 and DCC 077 were included in the catalogue even though they are not gravitationally bound structures yet, but they have enough mass and density contrast –with respect to the local environment and the critical density of the Universe– to have already detached from cosmic expansion and it is very likely that they will begin a process of collapse in the future.

Several of the structures compiled in the DCC catalogue correspond to identified *cores* of known superclusters already reported in the literature. For example, for the *Shapley Supercluster* (MSCC 389 and MSCC 401), one of the densest superclusters in the Local Universe, we have identified three *cores*: DCC 066, DCC 067 and DCC 068. The second one corresponds to the so-called 'central region' of *Shapley* (*e.g.*, Breen et al. 1994; Bardelli et al. 2000; Quintana, Carrasco, and Reisenegger 2000), a well-studied concentration consisting mainly of the Abell clusters A3556, A3558 and A3562 (see Figure 12). The other two structures identified here also correspond to important galaxy concentrations in *Shapley* reported in the literature (*e.g.*, Quintana, Carrasco, and Reisenegger 2000), consisting mainly of clusters A3528, A3530 and A3532, as well as A3571, A3572 and A3575, respectively (identified as MSCC 401 in Chow-Martínez et al. 2014). The DCC 066 and 067 *cores* correspond to the cluster complexes dominated by A3528 and A3558 as reported in Bardelli et al. (2000), with masses of $5.14\times10^{15}h_{70}^{-1}\mathcal{M}_{\odot}$ and $7.71\times10^{15}h_{70}^{-1}\mathcal{M}_{\odot}$, respectively, which is consistent with our estimates (see Table 5). The structures DCC 066, 067 and 068, constituted by well-known rich clusters, are clearly very massive and dense *cores* ($\delta_{\rm g}^{c}>9$, $\mathcal{R}>30$ and $\Delta_{\rm cr}>18$) in process of collapse, in agreement with Chon, Böhringer, and Zaroubi (2015).

For the *Corona-Borealis Supercluster* (MSCC 463), the most distant of the best-known superclusters, there is good agree-

d. The NASA/IPAC Extragalactic Database (NED) is funded by the National Aeronautics and Space Administration and operated by the California Institute of Technology. Website: https://ned.ipac.caltech.edu/.

https://doi.org/10.1017/pasa.2024.49 Published online by Cambridge University Press

Table 4. The Density-based *Core* Catalogue (DCC)

Name	ID	RA	Dec	$\bar{z}$	RA_{CM}	Dec_{CM}	z_{CM}	RA_{MMC}	Dec_{MMC}	$\bar{z}_{MMC}$	N_g	m_r		Cluster/group matches[2,3]
core	MSCC[1]	[deg]	[deg]		[deg]	[deg]		[deg]	[deg]				MMC	Other *core* members
(1)	(2)	(3)	(4)	(5)	(6)	(7)	(8)	(9)	(10)	(11)	(12)	(13)		(14)
DCC 001	1	0.748	-27.384	0.0646	0.748	-27.353	0.0646	0.754	-26.874	0.0654	236	2	A2716	S0003
DCC 002	1	2.491	-28.378	0.0612	2.847	-28.742	0.0612	3.066	-28.890	0.0610	251	5	A2734	A2726A
DCC 003	1	359.439	-31.850	0.0588	359.261	-32.186	0.0598	358.819	-32.902	0.0590	219	9	-	-
DCC 004	27	9.059	-25.705	0.0634	9.288	-25.649	0.0633	9.527	-25.367	0.0629	189	8	A2800	A0080A, EDCC 457, SWXCS J003759-2504.4
DCC 005	16/33	4.185	-31.376	0.1068	4.185	-31.376	0.1066	4.163	-31.351	0.1064	174	7	A2751B	A2759A
DCC 006	33	5.610	-33.756	0.1086	5.755	-33.835	0.1086	5.717	-33.338	0.1099	96	5	-	-
DCC 007	33	9.562	-28.739	0.1124	9.484	-28.759	0.1124	9.953	-28.903	0.1131	194	6	A2801	A2798B, A2804
DCC 008	33	10.257	-26.428	0.1121	10.146	-26.327	0.1123	9.962	-26.181	0.1124	89	4	EDCC 470	A0088
DCC 009	33	10.740	-28.532	0.1082	10.647	-28.528	0.1078	10.626	-28.547	0.1076	177	6	A2811B	A2814B
DCC 010	39	10.431	-9.470	0.0549	10.420	-9.520	0.0547	10.467	-9.303	0.0555	65	2	A0085A	SDSSCGA 00037
DCC 011	39	15.234	-14.992	0.0543	15.571	-15.081	0.0542	17.408	-15.437	0.0538	86	5	A151B	A126A
DCC 012	55	18.255	14.411	0.0594	18.050	14.182	0.0588	17.715	14.054	0.0579	192	7	A0150	A0152A, A160B, RXC J0110.0+1358
DCC 013	72	20.475	0.054	0.0777	20.421	-0.007	0.0777	20.272	0.045	0.0775	154	8	A0181A	SDSSCGB 07949
DCC 014	72	23.519	-0.078	0.0799	23.572	-0.101	0.0801	22.841	0.519	0.0794	248	6	A0208A	-
DCC 015	117	53.481	-53.352	0.0604	53.712	-53.160	0.0599	52.608	-52.599	0.0598	146	4	A3128B	A3125A, A3158, S0366, RXC J0334.9-5342
DCC 016	175	126.026	18.849	0.0979	126.069	19.291	0.0975	126.070	19.322	0.0975	106	3	A0659	A650B, MSPM 04607, SDSSCGB 68634
DCC 017	184	132.464	29.706	0.1043	132.285	29.651	0.1043	131.852	29.882	0.1049	93	3	A0705A	SDSSCGA 00018
DCC 018	219	152.862	19.169	0.1133	152.639	18.887	0.1134	152.408	18.560	0.1132	202	3	A0938B	A0942A, A0952A
DCC 019	222	156.006	49.460	0.1403	155.922	49.178	0.1420	155.893	49.078	0.1426	82	2	A0990	SDSSCGB 03458
DCC 020	iso/222	158.128	53.074	0.1369	158.363	52.824	0.1371	158.405	52.779	0.1371	57	3	WHL J103344.3+524855	A1027B, SDSSCGB 58169
DCC 021	236	151.972	15.114	0.0292	150.397	15.228	0.0295	149.939	15.473	0.0295	147	4	-	-
DCC 022	236	157.472	12.999	0.0325	157.725	13.661	0.0325	155.751	12.938	0.0320	230	8	A1016A	A0999A, A1020A, SDSSCGB 08731, SDSSCGB 11341
DCC 023	236	164.876	9.819	0.0350	165.012	9.978	0.0352	165.197	10.397	0.0354	153	4	A1142A	SDSSCGB 27956, USGC U339
DCC 024	278/236	173.329	22.675	0.0338	173.765	22.423	0.0326	172.261	22.900	0.0323	176	7	A1179B	A1177B, SDSSCGB 66609, MSPM 00173
DCC 025	238	155.446	41.292	0.0936	155.478	41.118	0.0927	155.040	41.011	0.0924	93	4	A0971A	SDSSCGB 40601, SDSSCGB 58543
DCC 026	238	156.534	37.597	0.1062	157.053	37.855	0.1050	157.184	37.919	0.1046	116	2	A1021B	A0995A, A0997B
DCC 027	238	157.984	35.713	0.1236	157.995	35.183	0.1233	157.917	35.022	0.1233	125	5	A1033	A1055, RXC J1031.7+3502, SDSSCGB 66740
DCC 028	iso/238	162.261	31.726	0.1145	162.349	31.776	0.1143	162.558	31.891	0.1138	81	2	MSPM 07607	A1097, SDSSCGB 07211
DCC 029	266	166.798	12.581	0.1261	166.786	12.632	0.1261	166.209	12.545	0.1277	99	3	A1159	A1152, A1183A, SDSSCGA 01118
DCC 030	272	167.795	40.530	0.0753	167.886	40.519	0.0753	167.993	40.717	0.0751	401	5	A1190	A1173, A1187, A1203, SDSSCGB 30685
DCC 031	277	169.329	53.424	0.1060	169.200	53.431	0.1063	168.962	52.838	0.1077	159	3	A1218B	A1225, SDSSCGB 02502, SDSSCGB 24283
DCC 032	277	169.470	47.387	0.1119	169.768	47.573	0.1119	170.338	47.937	0.1121	181	4	A1227A	A1202B, A1222, SDSSCGB 03830
DCC 033	277	170.846	49.265	0.1108	170.808	49.410	0.1106	170.566	49.801	0.1111	115	3	A1231A	WHL J112427.3+485246
DCC 034	278	167.072	28.433	0.0335	167.676	28.085	0.0337	167.651	28.585	0.0329	360	4	A1185A	SDSSCGB 11612, SDSSCGB 15832, SDSSCGB 41057
DCC 035	278	173.385	22.446	0.0335	173.627	22.273	0.0335	173.633	22.266	0.0335	233	3	A1267A	SDSSCGB 66609
DCC 036	278	178.128	20.472	0.0241	177.170	20.583	0.0243	177.716	21.068	0.0246	399	5	-	RXC J1204.1+2020, SWXCS J120409+2020.9
DCC 037	283	172.040	17.496	0.1294	171.897	17.270	0.1292	171.797	17.119	0.1289	65	3	A1264B	-
DCC 038	283	172.526	20.157	0.1332	172.530	20.192	0.1333	172.553	20.427	0.1335	90	2	A1278	A1274
DCC 039	283	172.700	24.146	0.1366	172.406	23.938	0.1369	172.369	23.856	0.1369	75	3	A1272	A1268, MSPM 08938
DCC 040	295	177.533	21.403	0.0229	177.133	20.889	0.0227	176.130	19.926	0.0216	727	7	A1367	-
DCC 041	295	191.864	27.017	0.0235	192.734	27.521	0.0234	194.777	27.862	0.0233	1193	6	A1656	[EKL2017] ECO0162, [EKL2017] ECO0207
DCC 042	310	152.062	53.943	0.0460	151.735	54.015	0.0462	152.414	54.420	0.0460	192	6	-	-
DCC 043	310	171.460	54.518	0.0696	171.062	54.467	0.0695	168.905	54.509	0.0699	258	5	RXC J1115.5+5426	A1270
DCC 044	310	178.083	54.588	0.0611	177.909	54.603	0.0611	177.058	54.643	0.0603	209	5	A1383	A1396A, A1400B
DCC 045	310	179.455	54.959	0.0509	178.163	55.343	0.0514	176.806	55.693	0.0518	270	7	A1377	A1324A, A1400A
DCC 046	310	181.666	56.943	0.0636	180.979	56.666	0.0642	180.070	56.204	0.0649	221	6	A1436	-
DCC 047	311	174.837	13.478	0.0813	174.117	13.845	0.0810	173.270	14.457	0.0812	333	6	A1307	-
DCC 048	311	175.230	11.494	0.0815	175.093	11.209	0.0812	175.078	10.903	0.0813	134	3	A1342A	A1337A
DCC 049	311	177.739	12.261	0.0836	177.853	12.220	0.0833	177.493	12.305	0.0836	268	6	A1390	A1372A, A1385A, MSPM 04978
DCC 050	314	176.670	-1.306	0.0788	176.420	-1.707	0.0784	176.256	-1.992	0.0776	83	3	A1364A	A1376A, SDSS-C4 1293
DCC 051	317	176.126	-2.138	0.1209	176.186	-2.166	0.1209	176.425	-2.279	0.1206	57	2	A1373A	-
DCC 052	317	176.675	-1.007	0.1179	176.761	-0.929	0.1181	176.483	-1.184	0.1176	36	2	A1376C	-
DCC 053	323	179.073	24.399	0.1403	179.003	23.879	0.1405	178.821	23.496	0.1403	94	4	A1413B	NSC J115657+241425, MaxBCG J179.49080+24.93397
DCC 054	323	179.499	26.216	0.1386	179.596	26.243	0.1383	179.794	26.296	0.1379	44	2	A1425B	A1420C
DCC 055	323	180.793	27.960	0.1371	180.739	28.071	0.1366	180.780	28.534	0.1348	102	4	A1449B	A1455C, SDSSCGB 06034
DCC 056	333	179.076	32.151	0.0794	178.891	32.740	0.0792	179.466	33.683	0.0798	94	6	A1423A	A1427
DCC 057	333	180.356	29.677	0.0803	180.450	29.923	0.0805	180.672	29.048	0.0810	81	7	A1444B	A1431A, A1449A
DCC 058	335	182.989	30.298	0.0743	182.748	30.726	0.0746	182.714	30.887	0.0742	71	3	A1480B	A1478A, A1486A
DCC 059	311/343	177.234	10.623	0.0845	176.174	8.036	0.0841	177.021	7.983	0.0835	97	3	A1379	A1358A, Mr20:[BFW2006] 25481
DCC 060	343	182.284	15.300	0.0810	182.078	15.014	0.0806	182.033	14.951	0.0805	86	2	A1474	A1481A
DCC 061	343	184.937	14.081	0.0820	185.341	13.882	0.0818	185.470	13.779	0.0816	82	4	A1526C	A1499A
DCC 062	352/343	187.067	12.002	0.0851	187.429	11.720	0.0854	187.445	11.708	0.0853	143	2	A1552	-
DCC 063	360	185.255	63.344	0.1061	184.568	63.617	0.1060	184.719	63.503	0.1062	88	4	A1518A	A1539A, A1544A, SDSSCGB 16981
DCC 064	386	196.775	39.710	0.0712	197.138	39.605	0.0713	197.770	39.273	0.0725	296	8	A1691	A1680A
DCC 065	391/386	203.630	36.420	0.0595	203.733	36.351	0.0595	204.111	35.936	0.0597	139	6	-	A1749A

https://doi.org/10.1017/pasa.2024.49 Published online by Cambridge University Press

Table 4. *Continued*

Name	ID	RA	Dec	$\bar{z}$	RA_{CM}	Dec_{CM}	z_{CM}	RA_{MMC}	Dec_{MMC}	$\bar{z}_{MMC}$	N_g	m_i	Cluster/group matches[2,3]	
core	MSCC[1]	[deg]	[deg]		[deg]	[deg]		[deg]	[deg]				MMC	Other *cores* members
(1)	(2)	(3)	(4)	(5)	(6)	(7)	(8)	(9)	(10)	(11)	(12)	(13)		(14)
DCC 066	389	194.211	-30.698	0.0545	193.997	-30.135	0.0546	193.641	-29.063	0.0542	141	5	A3528	A3530, A3532
DCC 067	389	202.604	-31.075	0.0479	202.569	-31.614	0.0479	202.182	-31.563	0.0477	451	7	A3558	A3552, A3556, A3557A, A3559A, A3560, A3562
DCC 068	401/389	207.434	-32.631	0.0388	207.068	-32.904	0.0388	206.863	-32.962	0.0389	178	3	A3571	A3572, A3575
DCC 069	414	204.778	26.019	0.0752	204.982	26.247	0.0753	205.461	26.403	0.0751	225	6	A1775B	-
DCC 070	414	208.223	28.559	0.0760	208.827	28.130	0.0754	209.778	27.997	0.0751	349	7	A1831B	A1800, A1817A
DCC 071	414	208.723	27.350	0.0626	208.449	27.150	0.0625	207.242	26.693	0.0625	425	8	A1795	A1818A, A1831A, WHL J135524.9+264738
DCC 072	414	213.558	26.407	0.0705	212.826	26.197	0.0701	213.282	26.610	0.0694	150	4	A1886A	SDSSCGB 13608
DCC 073	414	213.864	30.358	0.0667	214.212	30.072	0.0670	215.058	30.397	0.0672	170	7	-	A1869A
DCC 074	419	212.108	6.732	0.1128	212.510	6.623	0.1132	212.832	6.594	0.1134	166	5	A1870	A1862, A1866A, WHL J141226.4+072020
DCC 075	419	213.883	6.526	0.1096	213.577	6.781	0.1096	213.485	6.856	0.1095	81	2	A1881	-
DCC 076	419	215.600	6.329	0.1132	215.720	6.177	0.1129	216.099	5.875	0.1124	83	3	WHL J142448.1+054809	-
DCC 077	430	218.071	25.557	0.0958	217.797	25.570	0.0956	217.734	25.658	0.0953	109	3	A1927	A1926A
DCC 078	430	219.279	24.530	0.0892	219.258	24.425	0.0894	219.230	24.283	0.0896	86	2	WHL J143758.3+240906	A1939A
DCC 079	440	223.173	21.962	0.1171	223.156	21.888	0.1168	223.539	21.978	0.1166	194	4	A1986	A1976, A1980, WHL J145513.4+222111
DCC 080	441	223.827	27.906	0.1253	224.154	27.903	0.1252	224.693	27.892	0.1249	66	2	A2005B	A1984, A1990A
DCC 081	454	221.279	10.496	0.0518	221.906	10.789	0.0521	222.171	11.264	0.0521	222	8	-	MSPM 01932
DCC 082	454	229.032	7.599	0.0450	229.228	7.536	0.0449	230.377	7.737	0.0445	337	8	A2063B	A2028A, A2040,B A2055A
DCC 083	454	230.508	4.306	0.0379	229.773	4.421	0.0381	228.211	4.488	0.0385	533	9	SDSS-C4 1053	-
DCC 084	454	230.527	3.536	0.0506	229.666	4.577	0.0492	229.927	4.076	0.0494	208	5	WHL J151903.5+042001	WHL J151704.0+051522
DCC 085	457	227.456	8.246	0.0791	227.277	8.265	0.0784	227.318	7.727	0.0772	305	6	A2028B	A2040C, MSPM 05893
DCC 086	457	228.045	5.240	0.0785	227.813	5.495	0.0785	227.743	5.857	0.0785	524	10	A2029	A2033C, WHL J151052.2+045204
DCC 087	457	231.024	7.498	0.0762	231.615	7.425	0.0760	232.621	7.968	0.0753	233	14	-	-
DCC 088	457	231.580	3.251	0.0848	231.141	2.933	0.0845	230.498	2.360	0.0847	213	7	WHL J152203.5+022455	A2082A, MSPM 05682, SDSS-C4 1070
DCC 089	460	228.638	33.971	0.1132	228.308	33.538	0.1137	227.524	33.520	0.1135	213	4	A2034A	WHL J151710.7+332153
DCC 090	460	230.412	31.983	0.1133	230.490	31.815	0.1131	230.703	31.163	0.1137	165	3	A2067B	A2062
DCC 091	460	230.927	29.656	0.1142	231.015	29.721	0.1137	231.084	29.892	0.1136	283	4	A2069	A2059B
DCC 092	463	230.572	31.115	0.0773	230.479	30.971	0.0771	230.357	30.675	0.0772	343	7	A2061A	A2067A, MSPM 03940
DCC 093	463	232.261	27.782	0.0721	231.322	27.765	0.0718	230.668	27.739	0.0719	431	5	A2065	A2089
DCC 094	463	232.793	30.003	0.0659	232.676	29.323	0.0654	231.894	28.621	0.0673	343	7	A2073A	A2079A, A2092A, WHL J152912.3+293823, MSPM 03789
DCC 095	463	236.133	35.188	0.0683	235.768	35.132	0.0680	236.205	36.131	0.0662	247	10	A2122A	A2106A, A2124, Mr20:[BFW2006] 33265
DCC 096	463	238.869	28.553	0.0781	238.996	28.469	0.0781	237.922	27.862	0.0784	282	7	WHL J155203.6+275200	MSPM 05829
DCC 097	458/474	230.182	7.473	0.0341	230.106	7.829	0.0343	230.746	8.610	0.0344	419	5	A2063A	A2033A, A2040A, A2052
DCC 098	474	237.025	9.212	0.0398	236.247	8.501	0.0401	235.814	8.157	0.0401	185	4	MSPM 00299	MSPM 00295
DCC 099	474	240.378	14.865	0.0361	240.839	16.056	0.0370	240.840	16.107	0.0374	1172	12	A2147	A2151, A2152A, A2153A, MSPM 00504
DCC 100	484	244.738	42.521	0.1362	244.812	42.508	0.1361	245.063	42.458	0.1353	43	4	A2179	A2172, A2183
DCC 101	509	297.799	-30.414	0.0199	297.177	-29.827	0.0200	297.886	-30.856	0.0205	77	3	-	-
DCC 102	509	302.530	-41.756	0.0188	302.928	-40.533	0.0186	304.737	-41.159	0.0182	98	4	RXCJ2018.4-4102	A3656
DCC 103	574	351.646	-24.333	0.1114	351.682	-24.281	0.1116	351.659	-24.056	0.1119	67	4	A2599B	A2601A, APMCC 894, EDCC 300
DCC 104	574	352.502	-29.706	0.1060	352.684	-29.877	0.1062	353.071	-30.161	0.1064	101	5	-	A4009, [RTL2009] 245
DCC 105	579	351.451	14.630	0.0420	351.171	14.745	0.0419	351.100	14.520	0.0416	280	6	A2593A	A2589

Table note

1 The separator '/' is used to indicate that the *core* belongs to the MSCC supercluster with ID number on the left side, although it was detected in the supercluster box with ID number on the right side. The above is due to the overlap of supercluster boxes in the region. The special cases with the abbreviation 'iso' on the left side correspond to structures that do not belong to any MSCC supercluster, they are isolated *cores*.

2 Used catalogues: Abell/ACO catalogues (Abell 1958; Abell, Corwin, and Olowin 1989), Edinburgh-Durham Cluster Catalogue (EDCC, *e.g.*, Lumsden et al. 1992), Wen, Han & Liu Cluster Catalogue (WHL, *e.g.*, Wen, Han, and Liu 2012), Multiscale Probability Mapping Group and Cluster Catalogue (MSPM, *e.g.*, Smith et al. 2012), SDSS Compact Group Catalogue (SDSSCGA and SDSSCGB, *e.g.*, McConnachie et al. 2009), UZC-SSRS2 Group Catalog (USGC, *e.g.*, Ramella et al. 2002), C4 Cluster Catalog (SDSS-C4, *e.g.*, Miller et al. 2005), Mr20 Group and Cluster Catalog (Mr20:BFW2006, *e.g.*, Berlind et al. 2006), Northern Sky Optical Cluster Survey (NSC, *e.g.*, Gal et al. 2003), MaxBCG Cluster Catalog (MaxBCG, *e.g.*, Koester et al. 2007), Meta-Catalogue of X-ray detected Clusters of Galaxies (MCXC, *e.g.*, Piffaretti et al. 2011), and *Swift* X-ray Cluster Survey catalogue (SWXCS, *e.g.*, Liu et al. 2015).

3 The capital letters (A, B, C...) at the end of the Abell/ACO cluster names are used to identify the different components of a cluster along the line-of-sight (that reflect the redshift information available in late 2012, see, for example, Andernach et al. 2005; Chow-Martínez et al. 2014).

https://doi.org/10.1017/pasa.2024.49 Published online by Cambridge University Press

Table 5. Basic properties estimated for DCCs

ID DCC (1)	$\sigma_{\upsilon_{sys}}$ [km s^{-1}] (2)	$\mathcal{M}^{c}_{ext}$ [$10^{14} h_{70}^{-1} \mathcal{M}_{\odot}$] (3)	r_G [h_{70}^{-1} Mpc] (4)	V_c [h_{70}^{-3} Mpc^3] (5)	$\rho_c = \mathcal{M}^{c}_{ext}/V_c$ [$10^{10} h_{70}^{2} \mathcal{M}_{\odot}$ Mpc^{-3}] (6)	$n_c = N_g/V_c$ [h_{70}^{3} Mpc^{-3}] (7)	δ^{c}_{g} (8)	$\mathcal{R}$ (9)	Δ_{cr} (10)	Bind. state[1] (11)	d_{CMs} [h_{70}^{-1} Mpc] (12)
001	255	30.80 ± 4.51	33.25	1868.8	164.8 ± 24.1	0.1263	2.22	17.31 ± 2.68	11.12 ± 1.77	B	17.48
002	125	22.53 ± 3.40	14.97	784.5	287.2 ± 43.4	0.3200	7.17	30.16 ± 4.81	20.12 ± 3.19	B	10.19
003	248	10.42 ± 1.22	15.92	304.3	342.5 ± 40.1	0.7197	17.38	35.97 ± 4.60	24.19 ± 2.95	B	14.59
004	217	7.10 ± 1.15	12.87	309.0	229.7 ± 37.3	0.6117	18.57	86.48 ± 15.90	15.89 ± 2.74	B	7.02
005	192	13.71 ± 2.77	14.11	580.1	236.4 ± 47.7	0.3000	11.68	31.49 ± 6.52	16.38 ± 3.51	B	48.23
006	269	9.09 ± 2.61	16.88	346.2	262.6 ± 75.6	0.2773	10.72	34.98 ± 10.19	18.31 ± 5.55	B	46.54
007	150	19.30 ± 3.45	13.87	514.3	375.3 ± 67.2	0.3772	14.95	50.00 ± 9.23	26.60 ± 4.94	B	15.08
008	65	6.41 ± 1.41	18.11	168.1	381.2 ± 84.4	0.5295	21.39	50.78 ± 11.48	27.03 ± 6.20	B	29.98
009	296	19.58 ± 2.98	38.47	566.7	345.5 ± 52.6	0.3123	12.21	46.02 ± 7.32	24.40 ± 3.87	B	14.71
010	197	18.48 ± 4.70	23.93	287.5	642.8 ± 163.6	0.2260	16.51	87.57 ± 25.04	46.27 ± 12.03	B	12.93
011	179	12.38 ± 2.18	29.11	432.1	286.4 ± 50.6	0.1990	14.41	39.02 ± 8.56	20.06 ± 3.72	B	18.33
012	261	17.49 ± 2.74	16.44	536.9	325.8 ± 51.0	0.3576	15.99	24.70 ± 5.95	22.96 ± 3.75	B	10.51
013	169	3.83 ± 0.61	14.02	141.9	269.6 ± 43.4	1.0851	38.31	24.62 ± 4.57	18.83 ± 3.19	B	28.80
014	312	14.25 ± 1.76	21.14	768.4	185.5 ± 23.0	0.3228	10.69	16.94 ± 2.62	12.64 ± 1.69	B	9.21
015	270	29.32 ± 5.06	27.95	1414.1	207.4 ± 35.8	0.1032	8.22	29.43 ± 6.23	14.25 ± 2.63	B	26.33
016	301	17.56 ± 3.36	64.03	347.6	505.3 ± 96.7	0.3050	18.84	94.95 ± 19.93	36.16 ± 7.11	U	14.48
017	161	10.29 ± 2.18	27.93	181.8	566.0 ± 120.0	0.5117	70.68	310.64 ± 75.46	40.62 ± 8.82	B	15.64
018	350	51.99 ± 7.83	38.47	1605.5	323.8 ± 48.8	0.1258	18.83	107.15 ± 19.90	22.81 ± 3.58	B	7.99
019	747	17.50 ± 4.64	10.38	852.6	205.3 ± 54.4	0.0962	8.20	46.63 ± 14.15	14.09 ± 4.00	U	18.64
020	19	15.19 ± 4.50	54.30	191.0	795.5 ± 235.7	0.2984	27.55	180.71 ± 59.80	57.49 ± 17.33	B	29.88
021	58	7.21 ± 1.76	26.85	375.2	192.0 ± 46.9	0.3918	7.52	19.66 ± 4.99	13.12 ± 3.45	B	27.41
022	167	5.07 ± 0.98	22.72	219.7	230.7 ± 44.7	1.0470	21.76	23.62 ± 4.86	15.96 ± 3.28	B	9.68
023	142	6.07 ± 1.33	27.33	161.5	376.0 ± 82.6	0.9476	19.60	38.49 ± 8.87	26.65 ± 6.07	B	20.81
024	593	28.49 ± 7.82	26.79	1614.9	176.4 ± 48.4	0.1090	1.37	18.06 ± 5.11	11.97 ± 3.56	B*	33.21
025	359	16.16 ± 3.70	19.61	267.4	604.3 ± 138.5	0.3477	71.06	482.08 ± 117.18	43.43 ± 10.18	B	58.86
026	481	41.88 ± 9.17	59.79	813.3	514.9 ± 112.8	0.1426	28.56	410.76 ± 95.92	36.86 ± 8.29	B*	10.80
027	228	18.93 ± 4.09	72.16	1097.8	172.5 ± 37.3	0.1139	22.60	137.60 ± 31.77	11.68 ± 2.74	B	76.75
028	212	11.27 ± 3.75	32.62	408.5	275.8 ± 91.8	0.1983	40.09	220.05 ± 75.35	19.28 ± 6.75	B	68.16
029	8	36.13 ± 7.62	40.19	794.2	455.0 ± 95.9	0.1247	6.35	31.09 ± 8.64	32.45 ± 7.05	B	5.60
030	94	18.12 ± 1.73	15.15	582.5	311.2 ± 29.7	0.6884	21.21	47.22 ± 6.28	21.88 ± 2.18	B	2.84
031	552	26.12 ± 5.12	28.41	1091.3	239.4 ± 46.9	0.1457	7.62	24.06 ± 5.28	16.60 ± 3.45	B*	29.81
032	66	14.88 ± 2.37	24.21	525.3	283.3 ± 45.2	0.3446	19.39	28.48 ± 5.34	19.83 ± 3.32	B	22.29
033	336	32.86 ± 6.34	34.31	1249.7	262.9 ± 50.7	0.0920	4.44	26.43 ± 5.72	18.33 ± 3.73	B	9.54
034	277	13.11 ± 1.22	22.94	417.3	314.2 ± 29.3	0.8627	30.38	78.86 ± 8.11	22.11 ± 2.15	B	14.05
035	33	28.63 ± 3.10	394.71	1037.8	275.8 ± 29.9	0.2245	7.17	69.23 ± 8.09	19.28 ± 2.20	B	12.21
036	120	9.37 ± 1.23	12.60	335.9	278.9 ± 36.7	1.1879	42.22	70.00 ± 9.70	19.51 ± 2.70	B	33.65
037	134	12.94 ± 3.12	38.81	174.3	742.3 ± 178.9	0.3729	71.65	267.95 ± 71.35	53.59 ± 13.16	B	40.86
038	115	24.93 ± 5.69	24.41	882.0	282.7 ± 64.5	0.1020	18.88	102.04 ± 25.98	19.79 ± 4.74	B	11.14
039	49	22.61 ± 5.16	112.77	471.7	479.2 ± 109.5	0.1590	29.98	172.98 ± 44.10	34.24 ± 8.05	B	32.23
040	198	20.80 ± 1.79	18.84	1077.9	193.0 ± 16.6	0.6744	7.52	18.58 ± 1.79	13.19 ± 1.22	B	10.24
041	103	25.91 ± 2.58	16.30	1094.5	236.7 ± 23.6	1.0900	12.77	22.79 ± 2.47	16.41 ± 1.73	B	17.60
042	297	7.57 ± 1.27	13.62	253.6	298.7 ± 50.4	0.7571	25.02	41.76 ± 7.23	20.96 ± 3.71	B	77.45
043	282	13.02 ± 1.79	27.16	601.9	216.3 ± 29.7	0.4286	13.73	30.25 ± 4.31	14.91 ± 2.18	B	37.74
044	40	15.94 ± 2.85	22.57	455.5	350.0 ± 62.6	0.4588	14.77	48.93 ± 8.94	24.73 ± 4.60	B	12.55
045	204	11.62 ± 1.66	17.12	621.1	187.1 ± 26.7	0.4347	13.94	26.16 ± 3.86	12.76 ± 1.96	B	40.37
046	351	13.88 ± 2.09	29.71	695.2	199.6 ± 30.1	0.3179	9.93	27.91 ± 4.33	13.68 ± 2.21	B	27.40
047	248	19.36 ± 2.11	26.02	1177.9	164.4 ± 17.9	0.2827	17.29	34.03 ± 4.16	11.09 ± 1.32	B	14.84
048	279	11.83 ± 2.15	25.75	304.1	388.9 ± 70.7	0.4406	27.51	80.51 ± 15.29	27.60 ± 5.20	B	9.55
049	240	19.65 ± 2.42	23.93	700.6	280.5 ± 34.5	0.3825	23.75	58.08 ± 7.82	19.63 ± 2.54	B	20.00
050	298	13.97 ± 3.62	46.08	374.2	373.4 ± 96.7	0.2218	0.87	4.75 ± 1.45	26.46 ± 7.11	B	7.84
051	82	20.25 ± 5.12	25.74	335.5	603.7 ± 152.6	0.1699	18.95	95.39 ± 27.86	43.39 ± 11.22	B	17.09
052	112	9.72 ± 3.21	26.52	106.8	910.5 ± 301.2	0.3372	38.59	143.87 ± 52.03	65.95 ± 22.15	B	26.58
053	453	38.06 ± 8.52	37.98	1293.7	294.2 ± 65.8	0.0727	6.34	48.07 ± 11.99	20.63 ± 4.84	B	25.04
054	198	5.81 ± 2.04	33.67	161.6	359.6 ± 126.4	0.2723	26.52	58.76 ± 21.65	25.44 ± 9.29	B	2.73
055	201	33.93 ± 6.74	30.36	609.6	556.5 ± 110.6	0.1673	15.91	90.95 ± 20.67	39.92 ± 8.13	B	22.57
056	88	5.59 ± 1.43	40.94	358.5	156.0 ± 39.9	0.2622	2.16	6.02 ± 1.79	10.47 ± 2.94	B	19.49
057	172	9.08 ± 4.21	27.35	290.9	312.2 ± 145.0	0.2784	2.36	12.04 ± 5.88	21.95 ± 10.66	B	7.94
058	269	8.16 ± 5.70	22.67	429.5	190.0 ± 132.7	0.1653	3.48	19.73 ± 14.06	12.97 ± 9.76	B	9.01
059	192	11.44 ± 2.92	53.24	252.0	454.1 ± 116.2	0.3850	3.92	14.97 ± 4.00	32.39 ± 8.54	B	34.34
060	138	8.89 ± 1.87	75.95	204.7	434.2 ± 91.6	0.4200	4.37	14.32 ± 3.22	30.93 ± 6.73	B	15.21

https://doi.org/10.1017/pasa.2024.49 Published online by Cambridge University Press

Table 5. *Continued*

ID	$\sigma_{\upsilon_{sys}}$	$\mathcal{M}^c_{ext}$	r_G	V_c	$\rho_c = \mathcal{M}^c_{ext}/V_c$	$n_c = N_g/V_c$	δ^c_g	$\mathcal{R}$	Δ_{cr}	Bind.	d_{CMs}
DCC	[km s^{-1}]	$[10^{14} h_{70}^{-1} \mathcal{M}_\odot]$	$[h_{70}^{-1}$ Mpc]	$[h_{70}^{-3}$ Mpc$^3]$	$[10^{10} h_{70}^{2} \mathcal{M}_\odot$ Mpc$^{-3}]$	$[h_{70}^{3}$ Mpc$^{-3}]$				state[1]	$[h_{70}^{-1}$ Mpc]
(1)	(2)	(3)	(4)	(5)	(6)	(7)	(8)	(9)	(10)	(11)	(12)
061	98	4.79 ± 1.07	28.40	186.3	257.1 ± 57.9	0.4401	4.63	8.48 ± 2.02	17.90 ± 4.26	B	20.58
062	78	9.24 ± 1.65	297.03	320.2	288.5 ± 51.8	0.4466	4.71	9.51 ± 1.86	20.21 ± 3.81	B	35.49
063	66	14.26 ± 3.56	22.98	253.8	562.0 ± 140.6	0.3468	52.40	421.72 ± 116.46	40.32 ± 10.34	B	20.37
064	286	31.93 ± 3.88	22.41	726.9	439.3 ± 53.4	0.4072	21.41	83.42 ± 11.80	31.30 ± 3.93	B	11.08
065	341	6.12 ± 1.28	16.88	233.1	262.5 ± 55.0	0.5964	31.82	49.85 ± 11.04	18.30 ± 4.04	B	46.65
066	188	18.36 ± 3.19	20.84	670.9	273.6 ± 47.6	0.2102	9.60	30.52 ± 5.55	19.12 ± 3.50	B	42.56
067	175	50.67 ± 4.63	13.74	1532.8	330.6 ± 30.2	0.2942	13.84	36.87 ± 3.89	23.31 ± 2.22	B	7.52
068	271	17.15 ± 2.89	35.32	539.7	317.8 ± 53.5	0.3298	15.63	35.44 ± 6.25	22.37 ± 3.93	B	34.90
069	112	13.29 ± 2.26	14.02	335.0	396.7 ± 67.5	0.6717	17.04	32.14 ± 5.60	28.17 ± 4.96	B	47.63
070	300	35.55 ± 4.18	32.55	1394.9	254.9 ± 30.0	0.2502	5.72	20.65 ± 2.55	17.74 ± 2.20	B	37.87
071	138	25.63 ± 2.71	24.90	1110.5	230.8 ± 24.4	0.3827	9.28	18.70 ± 2.10	15.97 ± 1.79	B	25.92
072	243	20.09 ± 3.67	27.89	454.9	441.7 ± 80.8	0.3298	7.86	35.79 ± 6.69	31.48 ± 5.94	B	12.35
073	282	13.01 ± 2.12	20.74	507.9	256.2 ± 41.7	0.3347	7.99	20.76 ± 3.47	17.84 ± 3.07	B	18.40
074	159	24.37 ± 4.40	29.26	800.9	304.3 ± 55.0	0.2073	9.92	22.36 ± 4.59	21.38 ± 4.04	B	7.75
075	9	12.35 ± 3.04	80.82	178.7	691.1 ± 170.6	0.4533	22.88	50.78 ± 13.48	49.82 ± 12.54	B	11.42
076	196	15.61 ± 4.05	36.29	416.3	375.0 ± 97.2	0.1994	9.50	27.56 ± 7.64	26.58 ± 7.15	B	24.03
077	339	7.06 ± 1.43	20.37	319.0	221.2 ± 45.1	0.3416	24.01	43.65 ± 9.85	15.26 ± 3.31	U	10.03
078	146	10.32 ± 2.27	24.35	149.4	691.0 ± 152.0	0.5757	41.15	136.35 ± 32.76	49.81 ± 11.17	B	27.00
079	187	26.61 ± 3.51	29.16	867.8	306.6 ± 40.5	0.2236	19.87	89.65 ± 14.15	21.55 ± 2.98	B	7.14
080	108	14.10 ± 3.69	66.33	426.1	330.9 ± 86.7	0.1549	30.36	281.88 ± 100.81	23.33 ± 6.38	B	1.97
081	237	9.43 ± 1.53	14.96	555.9	169.6 ± 27.5	0.3994	16.82	24.48 ± 4.13	11.47 ± 2.02	B	43.97
082	242	15.33 ± 1.64	18.12	551.3	278.2 ± 29.7	0.6113	26.27	40.14 ± 4.68	19.45 ± 2.19	B	4.73
083	189	23.47 ± 2.49	15.68	764.0	307.2 ± 32.6	0.6976	30.12	44.33 ± 5.14	21.59 ± 2.40	B	25.98
084	187	30.54 ± 4.41	22.32	674.2	453.0 ± 65.4	0.3085	12.76	65.37 ± 9.92	32.31 ± 4.81	B	23.54
085	316	24.37 ± 2.82	18.91	785.7	310.2 ± 35.9	0.3882	17.01	31.76 ± 4.07	21.81 ± 2.64	B	20.37
086	226	40.15 ± 3.81	21.97	1155.3	347.6 ± 33.0	0.4536	20.04	35.58 ± 3.91	24.56 ± 2.43	B	10.65
087	269	13.49 ± 2.04	17.35	936.5	144.1 ± 21.8	0.2488	10.54	14.75 ± 2.37	9.60 ± 1.60	B	20.44
088	216	33.02 ± 4.74	27.95	838.6	393.7 ± 56.5	0.2540	10.78	40.30 ± 6.20	27.95 ± 4.15	B	28.77
089	259	43.32 ± 6.34	44.57	1758.6	246.3 ± 36.1	0.1211	6.64	23.77 ± 3.81	17.11 ± 2.65	B	23.34
090	298	19.71 ± 3.29	34.21	807.3	244.2 ± 40.7	0.2044	11.90	23.57 ± 4.23	16.95 ± 2.99	B	8.37
091	305	40.68 ± 5.10	25.16	1149.5	353.9 ± 44.3	0.2462	14.53	34.16 ± 4.83	25.02 ± 3.26	B	13.79
092	496	32.56 ± 4.14	29.71	151.0	282.9 ± 35.9	0.2980	12.64	29.54 ± 3.95	19.80 ± 2.64	B	21.17
093	287	44.27 ± 5.53	26.98	1504.6	294.2 ± 36.8	0.2865	12.11	30.73 ± 4.05	20.64 ± 2.70	B	12.55
094	350	29.06 ± 4.13	25.66	1159.0	250.7 ± 35.6	0.2960	12.55	26.18 ± 3.88	17.44 ± 2.62	B	32.49
095	462	26.23 ± 4.33	27.58	1076.0	243.7 ± 40.2	0.2296	9.51	25.45 ± 4.34	16.92 ± 2.96	B	39.19
096	314	28.55 ± 4.22	20.03	504.8	565.5 ± 83.6	0.5586	24.57	59.05 ± 9.08	40.58 ± 6.15	B	36.61
097	68	11.91 ± 1.25	16.16	511.9	232.7 ± 24.5	0.8184	6.94	12.43 ± 1.41	16.11 ± 1.80	B	32.61
098	228	14.19 ± 2.40	24.49	566.7	250.4 ± 42.4	0.3265	2.17	13.37 ± 2.33	17.41 ± 3.11	B	27.40
099	514	38.34 ± 2.15	23.31	1149.6	333.5 ± 18.7	1.0195	8.89	17.81 ± 1.24	23.53 ± 1.38	B	4.70
100	250	7.63 ± 2.00	20.66	245.9	310.2 ± 81.4	0.1748	2.17	5.51 ± 1.73	21.81 ± 5.98	B	12.36
101	144	3.98 ± 1.12	21.22	83.7	475.9 ± 134.1	0.9199	61.98	215.58 ± 63.32	33.99 ± 9.86	B	21.94
102	99	4.64 ± 1.11	23.38	206.4	224.6 ± 53.7	0.4748	31.51	101.77 ± 25.78	15.52 ± 3.95	B	10.39
103	116	15.70 ± 4.11	19.74	179.2	876.0 ± 229.7	0.3738	37.38	346.99 ± 94.79	63.41 ± 16.89	B	44.06
104	58	13.45 ± 2.82	18.04	359.6	374.0 ± 78.6	0.2809	27.83	148.14 ± 33.14	26.50 ± 5.78	B	66.31
105	273	10.46 ± 1.25	13.92	256.0	408.9 ± 49.0	1.0939	110.41	202.00 ± 33.32	29.06 ± 3.60	B	18.09

Table note

1 Gravitational binding state. B: structure globally bounded, B*: only one galaxy system is not bounded to the complete structure, U: structure not bounded as a whole.

https://doi.org/10.1017/pasa.2024.49 Published online by Cambridge University Press

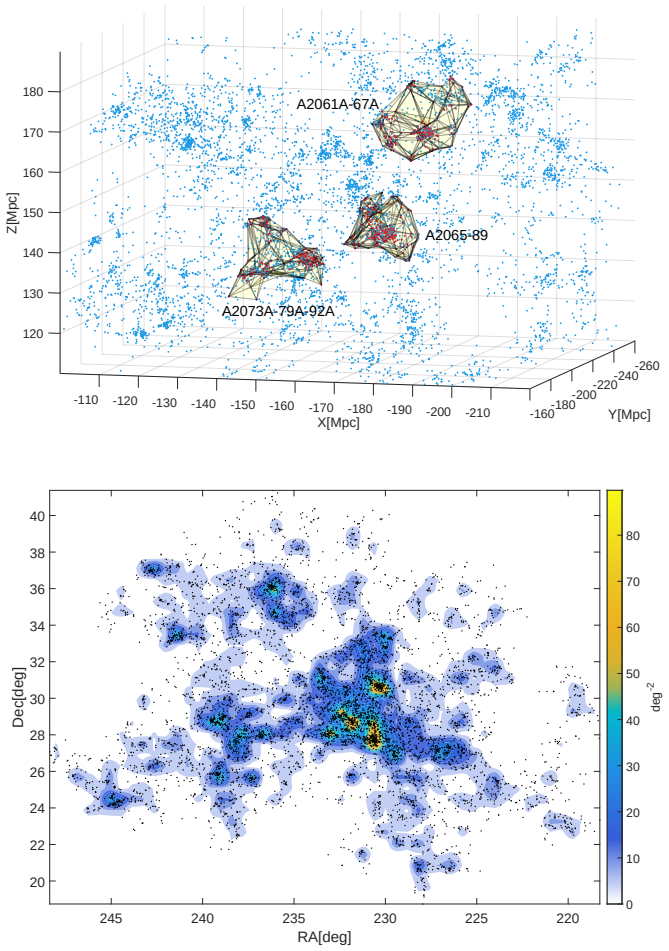

Figure 15. *Top:* The *Corona-Borealis Supercluster* (MSCC 463) and its three main *cores*: DCC 092 (A2061A-A2067A), DCC 093 (A2065-A2089) and DCC 094 (A2073A-A2079A-A2092A). These three *cores* were identified here as independent structures, but they could be a single central structure of the supercluster. *Bottom:* 2-D surface density map of the RA-Dec distribution of galaxies in the *Corona-Borealis Supercluster*. The three regions with the highest density of galaxies correspond to the DCC 092, DCC 093 and DCC 094 *cores*. The other two *cores* (DCC 095 and DCC 096) can be seen to the left (east) of the main concentrations. The density peaks correspond to the most massive clusters of each *core*.

ment between the detections made here and those reported in the literature: the so-called compact *core* of *Corona-Borealis* (*e.g.*, Small, Sargent, and Hamilton 1997; Small et al. 1998; Kopylova and Kopylov 1998; Marini et al. 2004), comprised by the A2061, A2065 (the richest dominant cluster), A2067, A2089 and A2092 clusters, appears here fragmented by DBSCAN into the DCC 092, DCC 093 and DCC 094 structures (see Figure 15). In fact, gravitational binding analysis (11) shows that these three structures are globally bound and density contrast analysis shows that the composite structure (DCC 092-093-094), with $\mathcal{R} \sim 29.22$ and $\Delta_{cr} \sim 19.41$, could constitute a single nucleation region that is already in a stage of collapse, in agreement with Small et al. (1998), Kopylova and Kopylov (1998), Pearson, Batiste, and Batuski (2014) and M. Einasto et al. (2021), who suggest that clusters A2061, A2065, A2067, A2089 and A2092, at the center of the supercluster, are in a stage of "rapid gravitational collapse" and will eventually form a large cluster. This cluster complex will likely become one of the most massive virialized systems in the nearby Universe (M. Einasto et al. 2021).

Two other *cores* worth mentioning are the structures DCC 040 and DCC 041 identified in the *Coma-Leo Supercluster* (MSCC 295) and containing, respectively, the very rich clusters A1367 and A1656 (see Figure 16). DCC 041 is the most prominent *core* of the supercluster and contains the Coma Cluster, A1656, one of the most studied in the Local Universe, while DCC 040 contains the Leo Cluster, A1367. As with the three main *cores* of the *Corona-Borealis Supercluster*, structures DCC 040 and DCC 041 can be connected by DBSCAN by expanding the neighborhood radius from 6 h_{70}^{-1} Mpc to as little as 6.5 h_{70}^{-1} Mpc. The two structures are connected by bridges of galaxy systems located between them, but are not gravitationally bound to any separate *core*. However, the composite structure, a large filament with densities $\mathcal{R} \sim 20.87$ and $\Delta_{cr} \sim 14.81$ seems to be globally bound and could be a single *core* for the *Coma-Leo supercluster* in a state of collapse, although no pairwise gravitational binding is verified between the Coma and Leo clusters. The three-dimensional distribution of galaxies in the *Coma-Leo Supercluster* allows us to appreciate that both DCC 040 and DCC 041 are located at the intersection of filamentary substructures, close to the estimated center of mass for the supercluster, so we may say that *Coma-Leo* presents a central binary *core*.

It is very interesting that the definitions of "quasi-spherical superclusters" (QSs) proposed by Heinämäki et al. (2022) goes in the same direction as our definition of *cores*. Of course our methods are different, but they give similar results, for example, for the masses of two objects we have in common: our DCC 046 (in the *Ursa Major Supercluster*, MSCC 310), with N_g = 221 and $\mathcal{M}^c_{ext} = (1.39 \pm 0.21) \times 10^{15} h_{70}^{-1} \mathcal{M}_\odot$, corresponds to its QS 524, with N_g = 283 and $\mathcal{M} = (1.82 \pm 0.64) \times 10^{15} h_{70}^{-1} \mathcal{M}_\odot$ centered on the A1436 cluster; and our DCC 097 (in the *Hercules Supercluster*, MSCC 474), with N_g = 419 and $\mathcal{M}^c_{ext} = (1.19 \pm 0.13) \times 10^{15} h_{70}^{-1} \mathcal{M}_\odot$, corresponds to its QS 550, with N_g = 680 and $\mathcal{M} = (2.58 \pm 0.73) \times 10^{15} h_{70}^{-1} \mathcal{M}_\odot$ around the A2052 cluster.

7. Discussion and conclusions

In this work we have identified *cores* in nearby rich superclusters through two consecutive percolation processes, one for galaxies and the other for systems in a three-dimensional space, combining the complementary FoF and DBSCAN clustering algorithms. *Cores* are understood here as gravitationally bound galaxy structures, comprised by two or more clusters and groups, with sufficient matter density to survive cosmic expansion and virialize in the future. The *cores* were selected from among several candidate structures –second-order galaxy 'clusters'– using density criteria (*e.g.*, Dünner et al. 2006; Chon, Böhringer, and Zaroubi 2015) that define them as nucleation

https://doi.org/10.1017/pasa.2024.49 Published online by Cambridge University Press

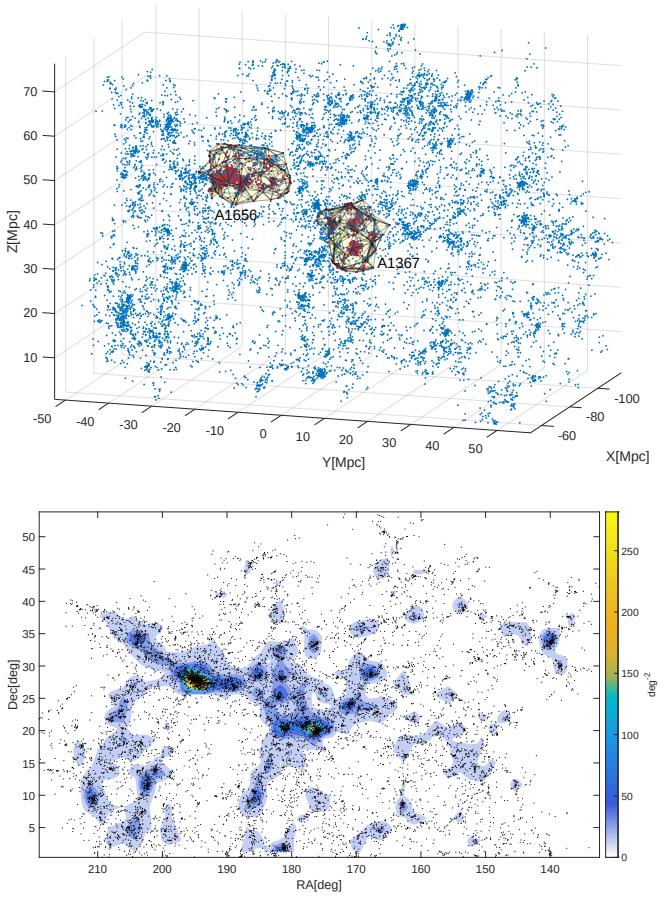

Figure 16. *Top:* The *Coma-Leo Supercluster* (MSCC 295) and its two *cores*: DCC 040 (A1367, Leo Cluster) and DCC 041 (A1656, Coma Cluster). These two *cores* were identified here as independent structures, but together they form a large filamentary structure that could be a single supercluster *core*. *Bottom:* 2-D surface density map of the RA-Dec distribution of galaxies in the *Coma-Leo Supercluster*. The two regions with the highest density of galaxies correspond to the DCC 040 and DCC 041 *cores*. The density peaks correspond to the most massive clusters of each *core* (as expected A1367 and A1656).

zones inside superclusters. In total, 105 structures were identified as *cores* whose galaxy samples are selected in the SDSS (main sample), 2dF and 6dF (complementary samples) regions. These *cores* and their estimated properties were compiled in the Density-based *Core* Catalogue (DCC) presented here.

Table 6 presents a summary of the ranges of values that the *core* properties compiled in Table 5 take, as well as their mean and median values. The mass and gravitational radius ranges of the DCCs are quite consistent with the mass and size ranges of the QSs of Heinämäki et al. (2022) and the high-density cores found by M. Einasto et al. (2016) for the Sloan Great Wall supercluster complex. In adittion, as can be seen from the mean/median values (see also Figure 17), the DCC-*cores* are structures that, in general, are already in the process of gravitational collapse since their density contrasts exceed the threshold values for structures at turn-around (*i.e.*, $\mathcal{R} \geq 12.15$ and $\Delta_{\rm cr} \geq 2.65$, according to Chon, Böhringer, and Zaroubi 2015) in the present epoch assuming a flat Universe with $\Omega_{m,0} = 0.3$ and $\Omega_{\Lambda,0} = 0.7$ (see also, Table 2). These values are expected to guarantee that most of these structures will virialize in the future, reaching some state of dynamical equilibrium regardless of their current evolutionary degree.

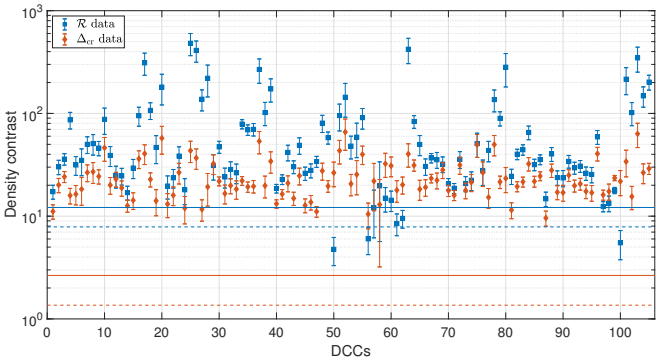

Figure 17. Density contrasts for DCCs. The horizontal axis shows the identifier of each core, while the vertical axis presents the two estimated values $\mathcal{R}$ and $\Delta_{\rm cr}$. The bars represent the propagated uncertainties. The blue and red dashed lines represent, respectively, the $\mathcal{R} = 7.86$ and $\Delta_{\rm cr} = 1.36$ values for structures prone to future collapse and the solid blue and red lines the respective $\mathcal{R} = 12.15$ and $\Delta_{\rm cr} = 2.65$ values for structures at turn-around in the present epoch.

We have shown that the distinct luminosity limits of our three sub-samples do not affect the detection of systems and their membership in SysCat, as can be seen from the comparison of our richness, masses, and mass uncertainties to the ones of similar system catalogues in the literature, since we optimized the use of the data for each supercluster box. Also, the relative mass error distributions for the SysCat systems show no significant trend within the redshift range of our supercluster sample ($0.02 \leq z \leq 0.15$), indicating that selection effects do not significantly affect our calculations of density contrasts. Furthermore, the mass and richness distributions of our systems are also quite consistent when compared to other catalogues, so the systems in SysCat are reliable. Furthermore, as explained in Section 5.3, the volumes of the structures were determined in such a way that they underestimated the density of the *core* candidates and overestimated the densities of their host superclusters, this being the worst-case scenario for *cores* selection. Even so, the selected structures presented high density contrasts with ranges of uncertainties that are within the established criteria as can be seen in Figure 17.

A preliminary topological analysis based on percolation reveals that, within superclusters, the *cores* are usually located at the intersections of large filaments, although *cores* can also be found as part of the latter or, less frequently, as isolated regions (*e.g.*, when they have cleaned/accreted most the matter around them) relatively close to the centers of mass of host superclusters. The mean and median values of the –Euclidean– 3D-distance, $d_{\rm CMs}$, between the centers of mass of the *cores* and those of their respective host superclusters are 23.4 h_{70}^{-1} Mpc and 20.4 h_{70}^{-1} Mpc, respectively. These centers of mass were estimated using the positions and virial masses of the member

https://doi.org/10.1017/pasa.2024.49 Published online by Cambridge University Press

Table 6. Outlier free range, mean (with standard deviation) and median (with the first-25% and third-75% quartiles) values for the basic properties estimated for the DCCs compiled in Table 5. The outliers were obtained by establishing the lower (Q1 – 1.5 × IQR) and upper (Q3 + 1.5 × IQR) limits, where IQR = Q3 – Q1 and is the interquartile range and Q1 and Q3 are the first and third quartiles of the data in the total sample. Once the outlier data below and above these limits have been removed, the quartiles of the refined sample are recalculated, which are shown here.

Core property	Range	Mean (± std)	Median (–Q1/+Q3)
Velocity dispersion of galaxy systems, $\sigma_{\upsilon_{sys}}$ [km s^{-1}]	[8, 514]	210 (±109)	203 (–77/+79)
Extensive mass, $\mathcal{M}^c_{ext}$ [$10^{14}h_{70}^{-1}\mathcal{M}_\odot$]	[3.83, 44.27]	18.34 (±10.10)	15.62 (–5.18/+9.80)
Gravitational radius, r_G [h_{70}^{-1} Mpc]	[12.60, 54.30]	25.51 (±9.24)	24.28 (–6.16/+4.98)
Volume, V_c [h_{70}^{-3} Mpc^3]	[83.7, 1614.9]	610.2 (±389.3)	514.3 (–210.1/+318.0)
Mass density, ρ_c [$10^{10}h_{70}^{2}\mathcal{M}_\odot$Mpc^{-3}]	[144.1, 604.3]	314.5 (±107.0)	291.3 (–51.9/+82.6)
Galaxy density, n_c [h_{70}^{3} Mpc^{-3}]	[0.0727, 0.7571]	0.3267 (±0.1597)	0.3085 (–0.1005/+0.0967)
Galaxy number density contrast, δ^c_g	[0.87, 42.22]	16.02 (±10.04)	14.42 (–6.37/+7.25)
Mass density excess (with respect to background), $\mathcal{R}$	[4.75, 148.14]	43.74 (±32.26)	32.14 (–8.77/+18.64)
Mass density contrast (with respect to critical density), Δ_{cr}	[9.60, 43.43]	22.13 (±7.87)	20.42 (–3.82/+6.07)

systems of each supercluster and each *core* from the SysCat catalogues (see columns from 2 to 4 of Table 3 and columns from 6 to 8 of Table 4). The location of the *cores* inside the superclusters depends mainly on the internal topology of the latter, which is closely related to their dynamical states (*e.g.*, Einasto, Saar, et al. 2007).

The main conclusions of this work are the following:

- Most of the rich superclusters (83% in the case of our sample) have high-density regions that can be identified as *cores*, structures characterized by having considerably larger concentrations of galaxies than other regions of the host superclusters and which can be considered as "nucleation zones" within the latter in the sense that they are structures that still accrete matter from their surroundings (e.g., filaments and the dispersed component of superclusters), concentrating it in more compact regions within which their member galaxy systems undergo mergers and great dynamical activity.
- Rich superclusters can have more than one *core*, and the number of these is proportional to the total mass and multiplicity of each host supercluster: superclusters with $\mathcal{M}^{sc}_{ext} \geq 10^{15}h_{70}^{-1}\mathcal{M}_\odot$ tend to have 3 or more *cores*.
- Within rich superclusters, *cores* are usually located at intersections of large filaments or forming part of these, although they can also be found, less frequently, in isolated regions (usually near the centers of mass of the superclusters), all depending on the internal topology —related to the dynamical state— of the host superclusters.
- *Cores* are structures made up of rich and poor clusters, small galaxy groups and dispersed galaxies frequently located in bridges that connect systems. They present with significant contrasts, δ^c_g, $\mathcal{R}$ and Δ_{cr}, with respect to the local number and mass densities as well as to the critical density of the Universe, respectively. The *cores* are themselves 'compact superclusters' extending to scales up to $\sim 15.0h_{70}^{-1}$ Mpc.
- *Cores* are the most massive and densest large-scale features that can be identified in the internal structure of rich superclusters. These are the largest gravitationally bound structures with a high probability of becoming virialized systems in the future which will survive the tear of cosmic expansion as 'island universes'.

Acknowledgement

The authors appreciate the material provided through private communication with Dr. Iris Santiago-Bautista. The authors are grateful for the discussions and suggestions of Dr. Varun Sahni and Dr. Satadru Bag that helped improve the volume estimates of structures through polyhedral surface fitting. The authors are grateful for the valuable suggestions of the anonymous referee that helped to improve the final version of this paper.

This research has made use of the VizieR catalogue access tool, CDS, Strasbourg, France (DOI: 10.26093/cds/vizier). The original description of the VizieR service was published by Ochsenbein, Bauer, and Marcout (2000).

This research has made use of the NASA/IPAC Extragalactic Database, which is funded by the National Aeronautics and Space Administration and operated by the California Institute of Technology.

Funding Statement This research was supported by CONAHCyT through a PhD grant and DAIP 0096/21 and 0162/22 projects grants.

Competing Interests 'None'.

Data Availability Statement Data resulted from the present work are available in the manuscript, both printed and digitally, and codes can be requested to the corresponding author.

References

Abdullah, M. H., G. Wilson, A. Klypin, L. Old, E. Praton, and G. B. Ali. 2020. *ApJS* 246:2.

Abell, G. O. 1958. *ApJS* 3:211.

Abell, G. O. 1961. *AJ* 66:607.

Abell, G. O., H. G. Jr. Corwin, and R. P. Olowin. 1989. *ApJS* 70:1.

Albareti, F. D., C. Allende Prieto, A. Almeida, and et al. 2017. *ApJS* 233:25.

Andernach, H., E. Tago, M. Einasto, J. Einasto, and J. Jaaniste. 2005. Nearby large-scale structures and the zone of avoidance. In *Asp conf. ser.* Edited by A. P. Fairall and P. A. Woudt, 329:283. San Francisco: Astron. Soc. Pac.

Araya-Melo, P. A., A. Reisenegger, A. Meza, R. van de Weygaert, R. Dünner, and H. Quintana. 2009. *MNRAS* 399:97.

Bahcall, N. A. 1996. Preprint (arXiv:astro-ph/9611148v1).

Bahcall, N. A., and R. M. Soneira. 1984. *ApJ* 277:27.

Bardelli, S., E. Zucca, G. Vettolani, and et al. 1994. *MNRAS* 267:665.

Bardelli, S., E. Zucca, G. Zamorani, L. Moscardini, and R. Scaramella. 2000. *MNRAS* 312:540.

Beers, T. C., K. Flynn, and K. Gebhardt. 1990. *AJ* 100:32.

Beers, T. C., M. J. Geller, and J. P. Huchra. 1982. *ApJ* 257:23.

Berlind, A. A., J. Frieman, D. H. Weinberg, and et al. 2006. *ApJS* 167:1.

Biviano, A., G. Murante, S. Borgani, A. Diaferio, K. Dolag, and M. Girardi. 2006. *A&A* 456:23.

Böhringer, H., and G. Chon. 2021. *A&A* 656:A144.

Böhringer, H., G. Chon, and J. Trümper. 2021. *A&A* 651:A16.

Bolton, A. S., D. J. Schlegel, E. Aubourg, and et al. 2012. *AJ* 144:144.

Breen, J., S. Raychaudhury, W. Forman, and C. Jones. 1994. *ApJ* 424:59.

Bryan, G. L., and M. L. Norman. 1998. *ApJ* 495:80.

Caretta, C. A., H. Andernach, M. Chow-Martínez, R. Coziol, J. De Anda-Suárez, Hernández-Aguayo C., and et al. 2023. *RMxAA* 59:345.

Caretta, C. A., M. A. Maia, W. Kawasaki, and C. N. A. Willmer. 2002. *AJ* 123:1200.

Chiueh, T., and X.-G. He. 2002. *Phys. Rev. D* 65:123518.

Chon, G., H. Böhringer, and N. Nowak. 2013. *MNRAS* 429:3272.

Chon, G., H. Böhringer, and S. Zaroubi. 2015. *A&A* 575:L14.

Chow-Martínez, M. 2019. Doctoral thesis, Universidad de Guanajuato, Mexico.

Chow-Martínez, M., H. Andernach, C. A. Caretta, and J. J. Trejo-Alonso. 2014. *MNRAS* 445:4073.

Coil, A. L. 2012. Large scale structure of the universe. Preprint (arXiv:1202.6633v1).

Cole, S., W. J. Percival, J. A. Peacock, P. Norberg, C. M. Baugh, C. S. Frenk, I. Baldry, J. Bland-Hawthorn, and et al. (2dFGRS team). 2005. *MNRAS* 362 (2): 505.

Colless, M., G. Dalton, S. Maddox, and et al. (the 2dFGRS team). 2001. *MNRAS* 328:1039.

Costa-Duarte, M. V., L. Sodré Jr., and F. Durret. 2011. *MNRAS* 411:1716.

Davis, M., G. Efstathiou, C. S. Frenk, and S. D. M. White. 1985. *ApJ* 292:371.

Dünner, R., P. A. Araya, A. Meza, and A. Reisenegger. 2006. *MNRAS* 366:803.

Edelsbrunner, H., and E. P. Mücke. 1994. *ACM Transactions on Graphics* 13 (1): 43.

Einasto, J. 2010. *AIP Conference Proceedings* 1205:72.

Einasto, J., M. Einasto, E. Tago, E. Saar, G. Hütsi, and et al. 2007. *A&A* 462:811.

Einasto, J., A. A. Klypin, E. Saar, and S. F. Shandarin. 1984. *MNRAS* 206:529.

Einasto, J., I. Suhhonenko, L. J. Liivamägi, and M. Einasto. 2018. *A&A* 616:A141.

———. 2019. *A&A* 623:A97.

Einasto, M., J. Einasto, E. Tago, V. Müller, and H. Andernach. 2001. *AJ* 122:2222.

Einasto, M., J. Einasto, E. Tago, E. Saar, L. J. Liivamägi, and et al. 2007. *A&A* 464:815.

Einasto, M., J. Einasto, P. Tejens, S. Korhonen, R. Kipper, E. Tempel, and et al. 2024. *A&A* 681:A91.

Einasto, M., M. Gramann, E. Saar, L. J. Liivamägi, E. Tempel, and et al. 2015. *A&A* 580:A69.

Einasto, M., R. Kipper, P. Tejens, H. Lietzen, E. Tempel, and et al. 2021. *A&A* 649:A51.

Einasto, M., H. Lietzen, M. Gramann, E. Tempel, E. Saar, L. J. Liivamägi, P. Heinämäki, P. Nurmi, and J. Einasto. 2016. *A&A* 595:A70.

Einasto, M., E. Saar, L. J. Liivamägi, J. Einasto, and et al. 2007. *A&A* 476:697.

Einasto, M., E. Saar, V. J. Martínez, J. Einasto, L. J. Liivamägi, and et al. 2008. *ApJ* 685:83.

Ester, M., H. P. Kriegel, J. Sander, and X. Xu. 1996. In *Kdd-96 proceedings,* 226.

Gal, R. R., R. R. De Carvalho, P. A. A. Lopes, and et al. 2003. *AJ* 125:2064.

Gramann, M., and I. Suhhonenko. 2002. *MNRAS* 337:1417.

Hambly, N.C., H.T. MacGillivray, M.A. Read, S.B. Tritton, E.B. Thomson, B.D. Kelly, D.H. Morgan, et al. 2001. *MNRAS* 326 (4): 1279.

Heinämäki, P., P. Teerikorpi, M. Douspis, P. Nurmi, M. Einasto M. ang Gramann, J. Nevalainen, and E. Saar. 2022. *A&A* 668:A37.

Hogg, D. W. 2000. Preprint (arXiv:astro-ph/9905116v4).

Huchra, J. P., and M. J. Geller. 1982. *ApJ* 257:423.

Jones, D. H., M. A. Read, W. Saunders, and et al. 2009. *MNRAS* 399:683.

Koester, B. P., T. A. McKay, J. Annis, and et al. 2007. *ApJ* 660:239.

Kopylova, F. G., and A. I. Kopylov. 1998. *AstL* 24:491.

Kriegel, H. P., P. Kröger, J. Sander, and A. Zimek. 2011. *Wiley Interdisciplinary Reviews: Data Mining and Knowledge Discovery* 1 (3): 231–240. https://doi.org/10.1002/widm.30.

Libeskind, N. I., R. van de Weygaert, M. Cautun, and et al. 2018. *MNRAS* 473:1195.

Liivamägi, L. J., E. Tempel, and E. Saar. 2012. *A&A* 539:A80.

Liu, T., P. Tozzi, E. Tundo, and et al. 2015. *ApJS* 216:28.

Łokas, E. L., and Y. Hoffman. 2002. Preprint (astro/ph0108283).

Lumsden, S. L., R. C. Nichol, C. A. Collins, and L. Guzzo. 1992. *MNRAS* 258:1.

Luparello, H., M. Lares, D. G. Lambas, and N. Padilla. 2011. *MNRAS* 415:964.

Marini, F., S. Bardelli, E. Zucca, and et al. 2004. *MNRAS* 353:1219.

MATLAB. 2023. *Matlab documentation: mathematics and optimization.* Available in: https://www.mathworks.com/help/index.html. The MathWorks, Inc.

McConnachie, A. W., D. R. Patton, S. L. Ellison, and L. Simard. 2009. *MNRAS* 395:255.

Melott, A. L., J. Einasto, E. Saar, and et al. 1983. *Phys. Rev. Lett.* 51:935.

Miller, C. J., R. C. Nichol, D. Reichart, and et al. 2005. *AJ* 130:968.

https://doi.org/10.1017/pasa.2024.49 Published online by Cambridge University Press

Nakamura, O., M. Fukugita, N. Yasuda, J. Loveday, J. Brinkmann, and et al. 2003. *AJ* 125:1682.

Ochsenbein, F., P. Bauer, and J. Marcout. 2000. *A&AS* 143:23.

Oort, J. H. 1983. *A&A* 21:373.

Pearson, D. W., M. Batiste, and D. Batuski. 2014. *MNRAS* 441:1601.

Peebles, P. J. E. 1980. *The large-scale structure of the universe.* Princeton, NJ: Princeton Univ. Press.

Peñaranda-Rivera, J. D., D. L. Paipa-León, S. D. Hernández-Charpak, and J. E. Forero-Romero. 2021. *MNRAS* 500 (1): L32.

Piffaretti, R., M. Arnaud, G. W. Pratt, E. Pointecouteau, and J.-B. Melin. 2011. *A&A* 534:A109.

Quintana, H., E. R. Carrasco, and A. Reisenegger. 2000. *AJ* 120:511.

Ragone, C. J., H. Muriel, D. Proust, and et al. 2006. *A&A* 445:819.

Ramella, M., M. Geller, A. Pisani, and L. Da Costa. 2002. *AJ* 123:2976.

Sander, J. 2011. Density-based clustering. In *Encyclopedia of machine learning,* edited by C. Sammut and G. I. Webb. Boston, MA: Springer. https://doi.org/10.1007/978-0-387-30164-8_211.

Sankhyayan, S., J. Bagchi, E. Tempel, S. More, M. Einasto, and et al. 2023. *ApJ* 958:62.

Santiago-Bautista, I., C. A. Caretta, H. Bravo-Alfaro, E. Pointecouteau, and H. Andernach. 2020. *A&A* 637:A31.

Sargent, W. L. W., and E. L. Turner. 1977. *ApJ* 212:L3.

Schneider, P. 2015. *Extragalactic astronomy and cosmology: an introduction.* Second. Springer.

Serna, A., and D. Gerbal. 1996. *A&A* 309:65.

Shandarin, S. F. 1983. *SvAL* 9:104.

Shandarin, S. F., J. V. Sheth, and V. Sahni. 2004. *MNRAS* 353:162.

Sheth, R., and A. Diaferio. 2011. *MNRAS* 417:4.

Small, T. A., C. P. Ma, W. L. W. Sargent, and D. Hamilton. 1998. *ApJ* 492:45.

Small, T. A., W. L. W. Sargent, and D. Hamilton. 1997. *ApJS* 111:1.

Smith, A. G., A. M. Hopkins, R. W. Hunstead, and K. A. Pimbblet. 2012. *MNRAS* 422:25.

Stauffer, D. 1979. *Phys. Rep.* 54 (1): 1.

Tempel, E., A. Tamm, M. Gramann, T. Tuvikene, L. J. Liivamägi, and et al. 2014. *A&A* 566:A1.

Theodoridis, S., and K. Koutroumbas. 2009. Pattern recognition. In *Pattern recognition, 4th edn.* Edited by T. Sergios and K. Konstantinos, 595. Boston: Academic Press.

Tully, R. B. 2015. *AJ* 149:54.

Tully, R. B., H. Courtois, Y. Hoffman, and D. Pomarède. 2014. *Nature* 513 (7516): 71.

Wen, Z. L., J. L. Han, and F. S. Liu. 2012. *ApJS* 199:34.

Zeldovich, Y. B., J. Einasto, and S. F. Shandarin. 1982. *Nature* 300:407.

Zúñiga, J. M., C. A. Caretta, A. P. González, and García-Manzanárez E. 2024. *RMxAA* 60:141.

https://doi.org/10.1017/pasa.2024.49 Published online by Cambridge University Press